Multi-site and Multi-vendor T2 Mapping from Proton Density and T2-Weighted Images

by

Gitanjali Chhetri

A thesis submitted in partial fulfillment of the requirements for the degree of

Master of Science

Department of Biomedical Engineering
University of Alberta

Abstract

Transverse relaxation (T2)-weighted images are routinely acquired in clinics. However, T2 quantification is rarely performed as most of the specialized pulse sequences used to quantify T2 are time consuming and thus generally not used in a clinical setup. Nevertheless, there is strong interest in quantitative measures in research settings. T2 quantification provides an unbiased measurement of tissue characteristics; it has been shown to be sensitive to a wide range of brain pathologies like Dementia, Multiple Sclerosis, Stroke, and Epilepsy, to name a few.

T2 measurement is commonly performed by curve-fitting an exponential decay to a long spin-echo train typically acquired from multiple-echo spin-echo sequences. However, errors arise from imperfect refocusing due to imperfect slice profiles and radio frequency interference effects at 3 T and higher fields. Imperfect refocusing leads to contamination of the T2 decay curve by contributions from stimulated and indirect echoes. Bloch equation-based modelling of the multi-echo spin-echo sequences have shown to provide accurate T2 measurements when a flip angle map is provided to the fitting method.

Large group MRI studies allow comparison of data across multiple sites and vendors, provided that the pulse sequences are standardized between the scan-

ner vendors and also between different scanner versions. This thesis is focused on testing the viability of using a T2 quantification method that can be applied across vendors and sites on existing clinical images. The method must make use of already acquired clinical images to ultimately enable clinical use without excessive sequence additions. Here we consider the proton-density and T2-weighted dual echo images for such T2 measurement. We examine retrospective T2 mapping across multiple sites and two vendors using only proton density and T2-weighted fast spin-echo images and an included calibration scan using the Alzheimer's Disease Neuroimaging Initiative (ADNI-1) database for healthy subjects at 3 T.

We show that a simple two-point exponential fit of these two images leads to striking biases in T2 measurements between vendors owing to differences in pulse sequence parameters. By using Bloch-based modelling of the pulse sequence and estimated $B1^+$ maps, these biases were removed.

The outcome of this work is that T2 quantification is possible from standard clinical images across sites and vendors if one models the actual pulse sequence and flip angles applied.

Preface

A version of Chapter 2 has been submitted to an academic journal. The research project makes use of retrospective in-vivo MRI data from the Alzheimer's Disease Neuroimaging Initiative (ADNI-1) database (**https://ida.loni.usc. edu/login.jsp?project=ADNI**) and volunteers scanned at the Peter Allen MR Research Centre.

The T2 fitting method used in the work was originally implemented by Kelly C. McPhee. I have made modifications in the simulation to accommodate ramped gradients for low SAR RF pulses. The fitting routine was also modified to speed up performance. The $B1^+$ map estimation pipeline is written by me. All other analysis on MRI data was performed by me.

The research projects, of which this thesis is a part, received research ethics approval from the University of Alberta Research Ethics Board, Project Name MRI in Neurological Disease Pro00000906.

To my parents and my brother

Acknowledgements

I would like to thank Dr. Alan Wilman for being supportive and understanding from day one. Working with him has been a wonderful experience. I have grown as a researcher and a person under his guidance. I would especially like to thank him for being patient with my progress during the pandemic. I feel fortunate to have him as my supervisor.

I would like to thank my committee, Dr. Richard Thompson and Dr. Atiyah Yahya, for their helpful feedback and comments. I would also like to thank Peter Šereš, Justin Grenier, Dr. Robert Stobbe, Karim Damji, and Dr. Graham Little for helping me out with MRI scans and neuroimaging softwares. I am also thankful to Dr. Kelly C. McPhee for her insightful review comments and suggestions. Although I have met her briefly once, I appreciate her sharing academic insights and some great career advice with me.

I am very thankful to all the friends I made in Edmonton. Life would have been hard without your friendship and cheerful presence. Missing home together made it less painful. Thanks to all my friends back home and abroad who pretended to listen when I tried explaining my research work to them. Thank you for never caring about time zones and waking me up at random times just to talk about the most random things. I am grateful to your price-

less friendships, shared experiences and beautiful memories.

Finally, I would like to thank my dad, mom, and brother, who are my biggest cheerleaders. Thank you for everything you do for me. I would not have been this far in life if it wasn't for your unconditional love and support.

Table of Contents

List of Tables

List of Figures

xv

Chapter 1

Introduction

1.1 Thesis Overview

Chapter 1 provides the necessary background to understand T2 modelling including basic introduction to magnetization, slice selection, T2 relaxation, methods for modelling and pulse sequences used. For background material a series of references used included the following [1–6].

Chapter 2 provides the research study on T2 mapping across vendors and sites, and Chapter 3 provides a brief conclusion, limitations and future directions.

1.2 Magnetic Resonance Imaging Background

The hydrogen proton is positively charged and possesses a property called spin. These protons act like tiny magnets. The sum of all the spins is called net magnetization ($\vec{M}$). Without a magnetic field, these spins would point in random directions and cancel out. In the presence of a main static magnetic field ($\vec{B}_0$), they align with and against the field. The direction parallel to $\vec{B}_0$ is the longitudinal or z-direction. Due to excess parallel spins, $\vec{M}$ is along the z axis and grows to a maximum value of $\vec{M}_0$. These protons precess about the

axis of $\vec{B}_0$ with a Larmor frequency,

$$\omega_0 = \gamma B_0 \tag{1.1}$$

where γ is the gyromagnetic ratio. The value of the gyromagnetic ratio for hydrogen ^{1}H is 4,258 Hz/G or 42.58 MHz/T.

A radiofrequency (RF) pulse is applied at the Larmor frequency and perpendicular to $\vec{B}_0$. As the protons absorb energy from this RF pulse, $\vec{M}$ rotates away from the z-direction and now precesses around $\vec{B}_0$ with two components: a longitudinal ($\vec{M}_z$) and transverse component ($\vec{M}_{xy}$) in the xy-plane. The amount of rotation (called as flip angle) depends upon the strength and duration of the RF pulse. When the RF pulse is turned off, the protons start to realign with $\vec{B}_0$ and give off energy while doing so. Another (or sometimes the same) RF coil detects this transverse component (NMR signal) as they oscillate at the Larmor frequency and it is converted to MR images using Fourier Transform. By applying much smaller magnetic field gradients in x, y, and z directions (with components in the z-direction), it is possible to spatially encode the signals, and after sufficient sampling, convert the data to images using the Fourier Transform.

1.3 Rotating Frame Of Reference

It is easier to understand MRI concepts in terms of a rotating frame of reference. If we consider the frame of reference rotating at the Larmor frequency, then the static magnetic field, $\vec{B}_0$ is not observed in the rotating frame and the transverse components of the magnetization $\vec{M}$ become static since they are precessing at the same Larmour frequency. During a RF field (B1), in the

2

rotating frame, $\vec{M}$ will precess around B1 with frequency,

$$f1 = \gamma B1 \tag{1.2}$$

However, if the B1 field is applied at a different frequency than the Larmor frequency, then the rotation during the B1 field gets more complex because the B1 is no longer static, and is most easily represented by using a rotating frame at the new B1 frequency during the RF pulse. Thus B1 is locked in the new rotating frame and effects of RF pulses can be easily understood.

1.4 Excitation

The process of rotating the net magnetization away from its equilibrium direction is called excitation. Excitation is achieved when a coil transmits a resonance RF field to the magnetization. This excitation field is also called the B1(t) field. Excitation is most easily understood in the rotating frame of reference, which precesses at the frequency of B1(t) rendering B1(t) to be static as shown in Figure 1.1.

The two main components of the B1(t) RF pulse are: (a) its frequency, which is generally tuned to the resonance.

The second major component is (b) the envelope of the B1(t) field, which includes both the strength and shape.

1.5 B1 field and Flip Angle

Flip angle is defined as the angle to which $\vec{M}$ is rotated relative to $\vec{B}_0$ via the application of the B1(t) field at the Larmor frequency. For a non-selective
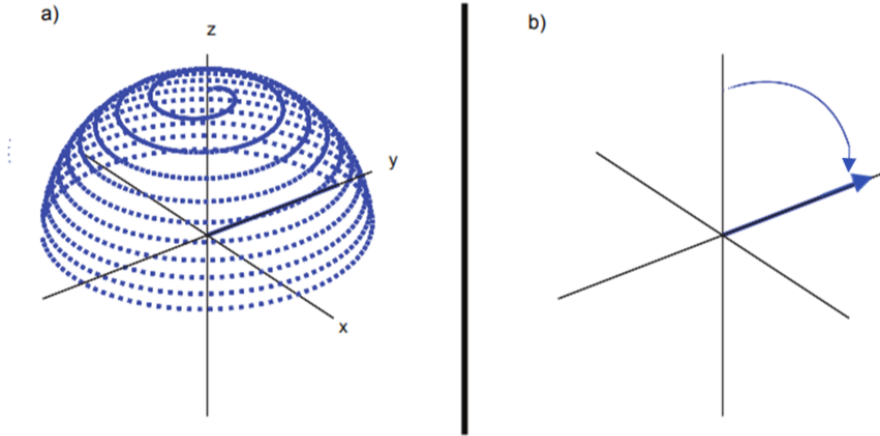
Figure 1.1: Excitation in (a) the laboratory reference frame and in (b) the rotating frame of reference, beginning with only longitudinal magnetization.

excitation, flip angle, α is given as:

$$\alpha = \int_0^T \gamma B_1(t)dt \qquad (1.3)$$

Different values of flip angle are obtained by modifying the area under the RF pulse envelope, either the strength of the B1 field, the length in time or the shape of the RF pulse envelope. In case of non-slice selective excitation and a rectangular pulse, the flip angle is directly proportional to the B1 value. For slice-selective excitation, however, the relationship is more complex. Slice selective excitation is a technique to specifically excite a slice. Slice thickness is given as:

$$Slicethickness = \frac{BW}{\gamma G_{ss}} \qquad (1.4)$$

where, BW is the bandwidth of the slice selective RF pulse and G_{ss} is the slice selection gradient amplitude. Slice-selective excitation is illustrated in Figure 1.2.

The technique relies on using an RF pulse with a constrained frequency

4
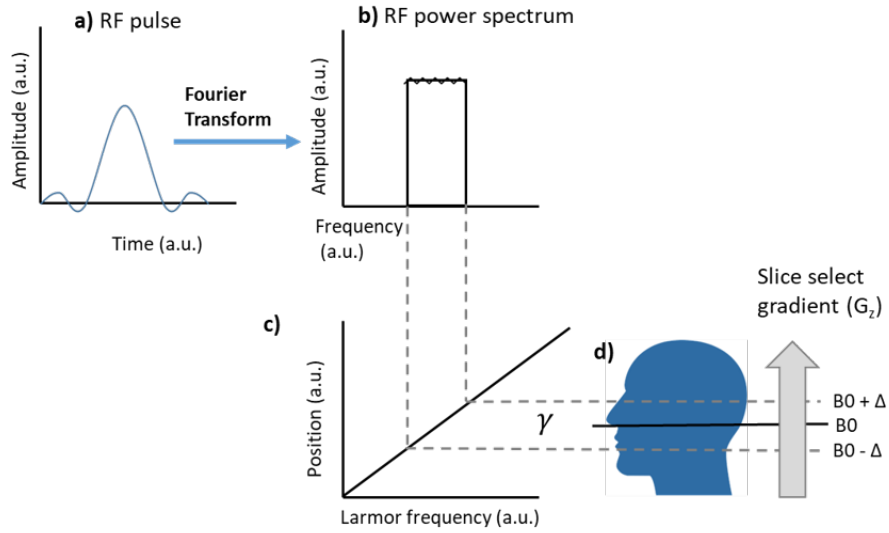
Figure 1.2: Slice-Selective Excitation. a) RF pulse envelope b) represents the frequency components of the excitation pulse calculated with the Fourier transform c) represents the frequency of the RF pulse related to the varying Larmor frequency which is proportional to the spatially varying magnetic field in part d).

spectrum and simultaneously applying a slice-select gradient which is applied along an axis perpendicular to the plane of the desired slice. This results in selective excitation of protons within the chosen slice. The slice-selective gradient causes the Larmor frequency to vary with position, and hence only the spins of interest within the RF frequency bandwidth are excited. Thus RF pulse and gradient are chosen such that it can excite the finite range of frequencies contained in the desired slice. Figure 1.2 demonstrates the mapping of the Larmor frequency to position with γ. The frequencies carried by an RF pulse can be roughly calculated by using a Fourier transform. Excitation occurs where the Larmor frequency of nuclei matches with the frequencies carried by the RF pulse. This is only an approximation and may introduce errors

in quantitative imaging that is discussed further in later sections.

1.6   Relaxation

After the B1 field is removed, the magnetization starts to return to equilibrium, with the longitudinal component regrowing and the transverse part dephasing. The time taken by the protons to return to equilibrium will depend upon the local environment. Energy may be lost. This energy loss happens in mainly two forms: from the spin system to the lattice and within the spin system itself. Two types of relaxation occur: Longitudinal relaxation (or T1) and Transverse relaxation (or T2). T1 relaxation time, also known as longitudinal relaxation time or spin-lattice relaxation time, is the time constant for the regrowth of the longitudinal magnetization ($\vec{M}_z$). It is the time required by the z component of M to reach 63% of its maximum value ($\vec{M}_0$). It involves energy transfer from a spin system to its surroundings (lattice).

1.7   Transverse Relaxation

Along with the recovery of the longitudinal magnetization, the transverse component decays simultaneously as a result of loss of phase coherence between the spins, also known as dephasing. Immediately after the RF excitation, the original distribution of the spins in the z-direction is preserved and transformed by rotation into "phase coherence" in the transverse plane. Soon after the excitation pulse is turned off there are two phenomenon that make the spins go out of phase: interaction between spins (irreversible process, characterized by transverse relaxation or T2 time) and $\vec{B}_0$ inhomogeneities (reversible process).

T2 or spin-spin relaxation time (Figure 1.3), is the loss of coherence in the precession of excited spins, causing a reduction in net transverse magnetization.

The origin of T2 relaxation is in variable magnetic fields that gives rise to dephasing of the transverse magnetization. The individual spins dephase with time as they experience locally fluctuating fields which are a combination of the static magnetic field $\vec{B}_0$ imperfections and the fields produced by their neighbors $(\vec{B}_0{}')$ resulting in different precessional frequencies. Over a time t, this creates a phase difference in precession proportional to $\vec{B}_0{}' t$ between the spin and its neighboring spins. Each spin develops such phase differences depending on the $(\vec{B}_0{}')$ experienced by it. This knocks the spins out of phase leading to each one precessing at a different rate and hence causing the T2 relaxation. This phenomenon is also referred to as the secular contribution to T2 relaxation.
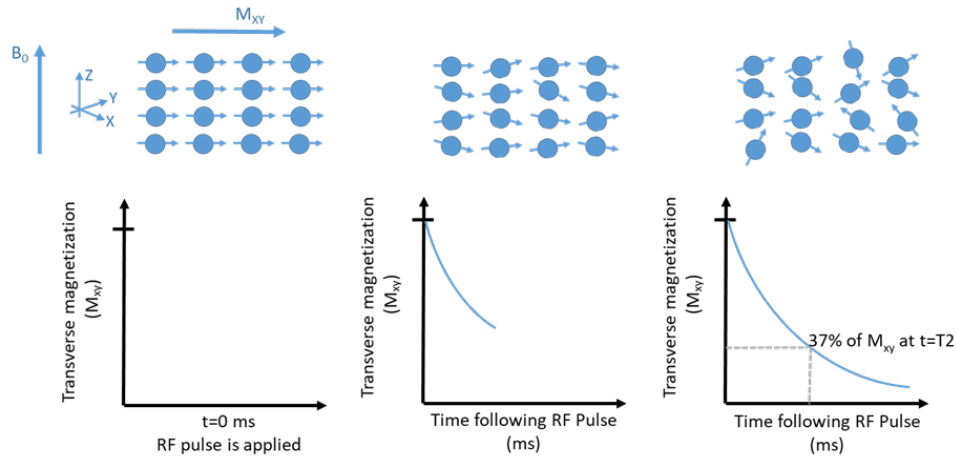
Figure 1.3: T2 relaxation process. Following a 90° excitation RF pulse the individual proton moments are tipped to the transverse plane and are in phase. Over time, this phase coherence is lost and the net transverse magnetization decays with rate 1/T2. Adapted from [7]

As well as dynamic field changes that affect T2, there can also be static field effects, which are refocused by a spin-echo but remain in a free induction decay. Multiple off-resonance effects including $\vec{B}_0$ imperfections, susceptibility differences between different types of tissues or at the tissue-air interfaces, and chemical shift lead to a faster dephasing. This observed rate is denoted as T2* or is also known as the effective T2 time. T2* is always less or equal to T2.

$$\frac{1}{T2^*} = \frac{1}{T2} + \frac{1}{T2'} \tag{1.5}$$

While the $T2'$ induced dephasing can be removed by applying 180° pulses (as in spin echo sequence discussed in section 1.9.1), T2 induced dephasing are irreversible since they are caused by random, local time-dependent field variations.

1.8 Bloch Equations including relaxation

The Bloch equation in its most simplest form is given by:

$$\frac{d\vec{M}}{dt} = \gamma \vec{M} \times \vec{B} \tag{1.6}$$

There are three relevant magnetic fields that add up to $\vec{B}$:

1. The static magnetic field, $\vec{B}_0$

2. The RF or $\vec{B}1$ field

3. Magnetic field gradient, $\vec{G}$

The Bloch equations including relaxation terms in the rotating frame are:

$$\frac{d\vec{M}}{dT} = \gamma \vec{M} \times \vec{B} - \frac{M_x \hat{x} + M_y \hat{y}}{T2} - \frac{(M_z - M_0)\hat{z}}{T1} \tag{1.7}$$

$\hat{x}, \hat{y}, and \, \hat{z}$ are unit vectors along x, y, and z axis respectively.

Considering transverse magnetization $M_{xy} = M_x + iM_y$, Equation 1.7 can be

solved for the relaxation times as:

$$M_z(t) = M_0 + [M_z(0) - M_0] \exp \frac{-t}{T1} \tag{1.8}$$

$$M_{xy}(t) = M_{xy}(0) \exp \frac{-t}{T2} \tag{1.9}$$

Where $M_{xy}(0)$ and $M_z(0)$ are the initial transverse and longitudinal components of magnetization at time zero and M_0 is the equilibrium magnetization.

1.9 Spin-echo Pulse Sequences

1.9.1 Spin-Echo

Originally proposed by Hahn [8], in a standard single-echo spin-echo (SE) sequence (Figure 1.4), a 90° RF excitation pulse is applied along the x direction which tilts M_z along the transverse plane. Once the RF pulse is withdrawn, the spins dephase due to T2 and $T2'$ relaxation mechanisms. After a time duration, τ, a 180° RF pulse is applied along the y direction which flips the precessing spins. The 180° pulse is known as the refocusing pulse. It effects a rephasing of the spins owing to a reversal of the $T2'$ decay such that a Hahn spin-echo is formed at a time, $TE = 2\tau$. The sequence then repeats at time TR, the repetition time. The spin-echo does not reverse the effect of the T2 signal loss. Ignoring diffusion effects, the magnitude of the echo peak is given as:

$$S = S_0 \exp \frac{-TE}{T2} \tag{1.10}$$

One way to measure the T2 is by performing a series of n single-echo SE experiments with varying echo times. However, due to the need for n separate image acquisitions, this method is slow. Also the increasing inter-echo time
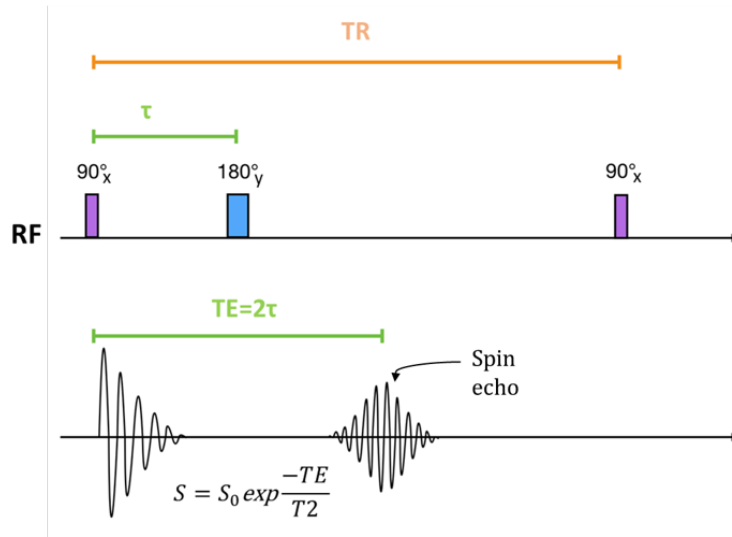
Figure 1.4: Pulse sequence diagram of the standard spin-echo sequence

between measures biases results to diffusion or other dynamic changes that may occur with longer inter-echo spacing [9, 10]. Faster T2 measurements are achieved using multi-echo spin-echo techniques. The most popular one is the Carr Purcell Meiboom Gill (CPMG) sequence discussed in the next section.

1.9.2 Carr Purcell Meiboom Gill Sequence

In multiple echo spin-echo (MESE) sequences, multiple refocusing pulses are applied successively to obtain the T2 decay signal at multiple echo times (TE) while keeping the inter-echo spacing constant. The Car Purcell Meiboom Gill pulse sequence [9, 10] is commonly used in T2 measurement. The main idea of the CPMG method is to apply the 180° pulse with a phase in quadrature with the 90° excitation pulse. The phase shift is intended to reduce the effects of imperfect 90° refocusing pulses. The $90°_x$ pulse flips the magnetization vector to xy plane. The spins dephase over time reducing the net transverse magne-
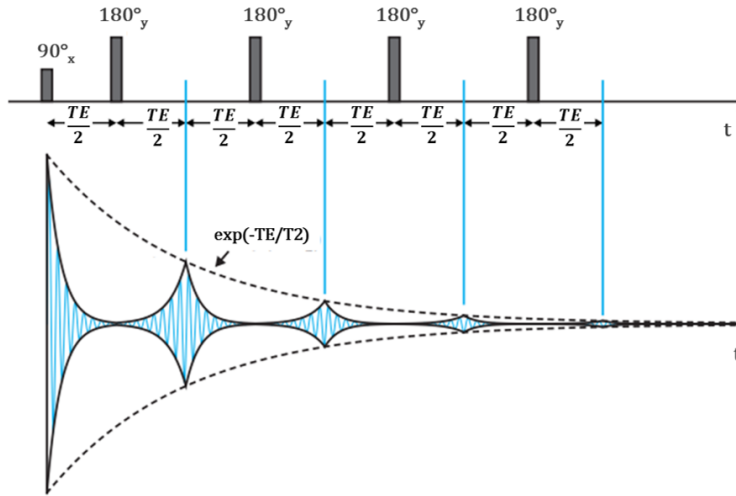
Figure 1.5: Pulse sequence diagram of a typical CPMG sequence. Multiple spin-echoes generated by a train of equally spaced 180° RF pulses. Adapted from [2]

tization. The dephasing due to the effects of magnetic field inhomogeneity are refocused by applying $180°_y$ pulses at TE/2, 3TE/2, 5TE/2...after the $90°_x$ pulse. spin-echoes are formed at TE, 2TE, 3TE..The intensity of the resulting echoes is used to measure T2 using Equation 1.10

1.9.3 Fast spin-echo

The fast spin-echo (FSE) or turbo spin-echo (TSE) or rapid acquisition with relaxation enhancement (RARE) technique [11] uses multiple refocusing pulses to generate multiple echoes per excitation pulse (Figure 1.6). The phase encoding gradient amplitude varies prior to each echo in the train so that each echo fills a different line of k space. Since multiple lines of k-space can be acquired in a single TR period, the FSE sequence significantly reduces the scan time. The number of echoes acquired in a given TR is called echo train length (ETL) or turbo factor. Increasing ETL reduces scan time. Additionally, longer ETL

also may mean a lower signal to noise ratio (SNR) and contrast to noise ratio (CNR). A long echo train also contributes to spatial blurring in the image. In the brain, common ETLs are 8-16. The time between the echoes is called echo spacing or ESP. Most vendors use the lowest possible ESP as increasing ESP gives rise to motion and susceptibility related artifacts thus compromising with the SNR and CNR of the images. The distribution of specific phase-encoding
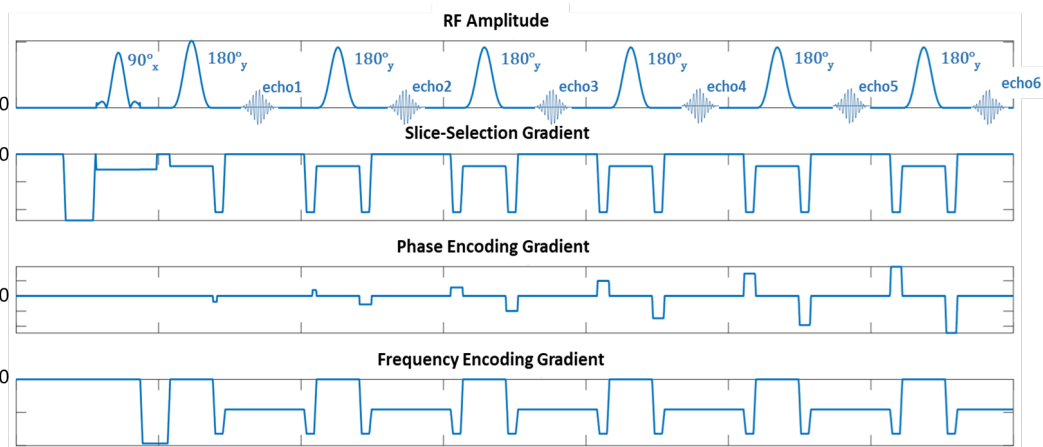
Figure 1.6: Pulse sequence diagram of a six echo fast spin-echo sequence

values to echoes in the train determines image contrast. Effective echo time, TE_{eff} is the echo time of the echo acquired with the smallest phase encoding value, often zero. This echo essentially determines the contrast of the image. In the case of dual-echo FSE images, central phase encodes are collects twice at both early and later stages of the FSE echo train to provide two effective echo contrasts, with middle echoes providing all the other phase encodings. This results in two sets of images: PD-weighted images corresponding to $TE1_{eff}$ and T2-weighted images corresponding to $TE2_{eff}$.

FSE can be used in 2D or 3D mode. The sequence generally uses a pair of gradient lobes on either sides of the slice selective refocusing RF pulses to

crush or rephase unwanted signal coming out of the slice of interest, or signal excited by one of the refocusing pulses. FSE is the most commonly used T2 weighted sequence in clinics because of its speed and high SNR.

Proton density (PD) refers to the concentration of visible hydrogen protons in tissue. When TSE scan parameters are set for short echo time and long repetition time, it is the dominant contrast. Note that all weighted images have intrinsic PD weighting, in addition to any other dependence on other tissue properties such as T1, T2 or diffusion. PD weighted images have a much higher SNR than T2-weighted images due to the short TE and corresponding long TR. Tissues with high PD tend to have high water content. Thus PD offers a means to observe high water content such as found in some MS lesions, abscesses and CSF. However, PD images are not that specific to subtle water content changes so are best paired with T2-weighted images as well. Historically, PD images were often acquired with T2-weighted spin echo images as a dual echo. The early echoes did not have T2 contrast, so could be used for PD.

In the brain, PD/T2 weighted images are part of the Canadian Dementia Imaging Protocol [12] and PD images are a recommended additional sequence in multiple sclerosis studies for brain [13]. In the spinal cord, PD-weighting becomes an essential sequence in Multiple Sclerosis, since its higher SNR enables discovery of subtle cervical cord lesions that might be difficult to depict on lower SNR T2-weighted images. Studies have shown that PD FSE is superior for the detection of cervical cord MS lesions [14] and periventricular lesions [15]. Lastly, PD weighted images have also shown to offer good signal distinction between fluid and cartilage, which makes it useful in the assessment of

joints [16]. For joints, the short TE of the PD images helps preserve rapidly decaying tissues, that might be severely reduced in a T2-weighted image.

1.10 Challenges in T2 Quantification

Relaxometry refers to measurement of the relaxation times from MR images. As mentioned, the gold standard for T2 relaxometry is MESE sequences. The multi-echo images from MESE data are used for fitting signal models to estimate the T2 of the measured signal [3]. The simplest approach involves fitting the exponential curve (Equation 1.10) to the acquired data points for each voxel. By converting voxel values to T2 times, quantitative T2 maps are obtained. This is also referred to as mono-exponential analysis. T2 quantification from MESE sequences has a reasonably straightforward implementation, however, there are several limitations to this approach in actuality. MR signals are sensitive to the flip angles of the excitation and refocusing RF pulses. In practice, the nominal flip angle always deviates from the actual flip angle in some regions of the volume. The most common causes being RF inhomogeneity, slice profile effects in case of slice selective pulses, and certain SAR related modifications to the MESE sequences.

1.10.1 RF or $B1^+$ inhomogeneity

The major source of transmit RF inhomogeneity is electromagnetic interactions of the RF waves with the object being scanned [17, 18]. With the increase in B_0 (typically at 3T and higher), the corresponding Larmor frequency for the $B1^+$ RF field also increases, causing $B1^+$ inhomogeneity problems in MRI. At high frequencies, the wavelength of the RF field is comparable to or less than

that of the dimension of the human body, as the permittivity of the tissues come into play. At 3T, a half-wavelength in the head is roughly 13 cm [19]. As a consequence, the RF magnetic field inside a sample exhibits stronger wave behavior than in air and is subjected to constructive and destructive interference. Waves arriving from different portions of the RF coil with equal path lengths to a specified location, will add constructively as expected, but when path lengths vary, signals can arrive with different phases, giving rise to signal loss. Thus the transmit RF field at the center of the coils is higher than at the sides of the coil. Figure 1.7 shows an example of RF field variation in human head at 3T.
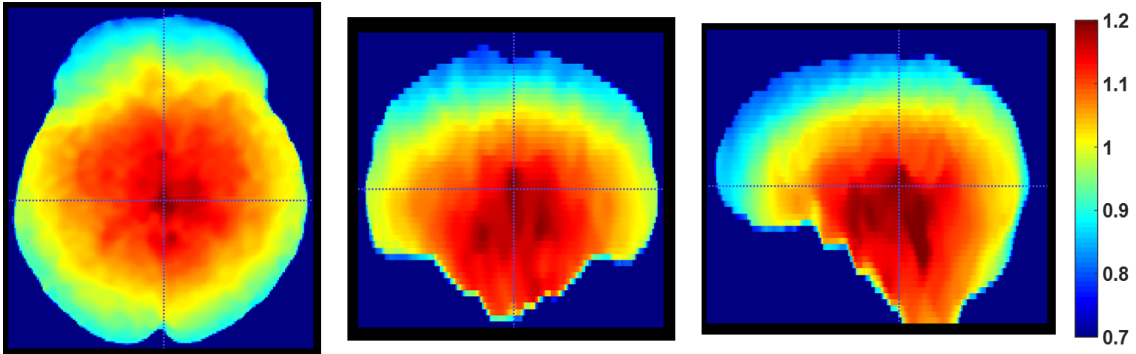
Figure 1.7: Normalized transmit RF field variation in human head at 3T collected with Bloch-Siegert $B1^+$ mapping. Over the whole brain, the mean value is near 1.0 receiving the nominal mean flip angle, but central regions are much higher while edge regions much lower.

Flip angle maps are crucial to many advanced T2 fitting methods and are generally acquired through additional scans, although the flip angle can also be included as an additional variable in the T2 fitting process, when there are enough data points collected. The sensitivity of the receive RF coil also impacts the signal intensity, but since T2 fitting is done voxel by voxel, the

receive signal only affects the SNR.

1.10.2 Specific Absorption Rate (SAR)

The application of RF pulses cause energy deposition in the tissue which leads to tissue heating. The heating is attributed to the interaction of the RF coil's electric field with the conductive tissue in the body. Specific absorption rate (SAR) is a measure of the amount of power deposited by a radiofrequency field in a certain mass of tissue [20] and is measured in W/kg. The standard limits are 3.2 W/kg for head with exposure averaged of 6 minutes [21]. SAR plays a key role in deciding pulse parameters. The SAR value is proportional to B_0^2, $B1^2$ and α^2.

In a sequence like FSE, repeated RF refocusing pulses lead to greater tissue heating. A longer echo train of RF pulses will increase the SAR value. SAR can be reduced by decreasing the number of slices acquired within one TR. The most common way to control SAR in FSE sequences is by reducing the amplitude of refocusing flip angle. However this comes at the expense of creating a more complex signal decay.

1.10.3 Magnetization Transfer

Magnetization transfer (MT) in biological tissues is generally attributed to the transfer of magnetization between different spin systems [22]; the two primary systems being composed of (a) relatively mobile bulk water molecules or a free proton pool, and (b) a relatively immobile water in the vicinity of the macromolecules or a bound proton pool. While T2 of a free proton pool is typically longer, the T2 associated with the bound proton pool is relatively

short but has a large range of resonant frequencies. The slice selective RF pulse in multi-slice imaging, acts as an off-resonant excitation pulse for the neighbouring slices. The bound spins are partially saturated with the off-resonant pulse and they exchange magnetization with the free water pool. Due to the very short T2 of the bound spins, this saturation is not directly visible. However it has been shown to affect image contrast in multi-slice MR imaging if there is sufficient transfer of energy between these two spin systems. Longitudinal spins in the free proton pool become saturated by exchanging with the spins that have been saturated by off-resonance pulse. The resulting effect is the apparent signal loss from the free proton pool. Stronger MT effects have been associated with longer ETL.

Studies have shown that MT effect varies due to B1 variation and local tissue sensitivity [23]. MT effect is found to be particularly stronger in tissues with high macromolecular content such as in white matter. The resulting effect is signal loss in the tissue [24]. T2 measurements using MESE sequences in single slice mode and 3D acquisitions are usually not affected by the MT effect.

1.10.4 Partial Volume Effects

The partial volume effect arises when different tissue types reside within an imaging voxel. The MR signal from such a voxel is a weighted average of signals from the different tissue types within that voxel. Opting for thinner slices lowers the partial volume effect, however, due to the millimetre spatial resolution of MRI it is practically impossible to fully remove partial volume artifact, since each voxel will contain many microscopic environments. As one example, the brain white matter has been shown to possess multiple T2

water pools [25] arising from water trapped in myelin layers and more free intra/extra cellular water. Multi-component T2 decay models are generally employed to analyze the individual contributions within a voxel. The multi-component T2 decay is an extremely ill posed problem. Many authors in the past have attempted different regularization terms in the estimation. A high SNR requirement of this model is the second major challenge. Differentiating T2 peaks from the multi-component T2 relaxometry is quite challenging at low SNRs.

The T2 fitting model employed in this work assumes mono-exponential T2 relaxation.

1.10.5   Stimulated Echoes

A spin-echo is formed by the 90°-180° pulse pair. Stimulated echoes arise when there are at least three RF pulses (except true 180°) where magnetization is stored in the longitudinal plane [26]. Consider the case of 90°-90°-90° RF pulses (Figure 1.8) The first pulse generates transverse magnetization, which is converted to longitudinal magnetization by the second pulse. This stored longitudinal magnetization is flipped back into the transverse plane by the third RF pulse that rephases and gives rise to a stimulated echo. The stimulated echo has both T1 and T2 weighting. Contributions from such alternate echo pathways result in higher signal of later echoes, causing T2 overestimation (Figure 1.9). Indirect and stimulated echoes are formed even when the nominal flip angles is equal to 180°, because in practice slice profiles are not perfectly rectangular. Vendors generally employ values lower than 180° to mitigate SAR issues. Non-rectangular slice profile in 2D imaging leads to a
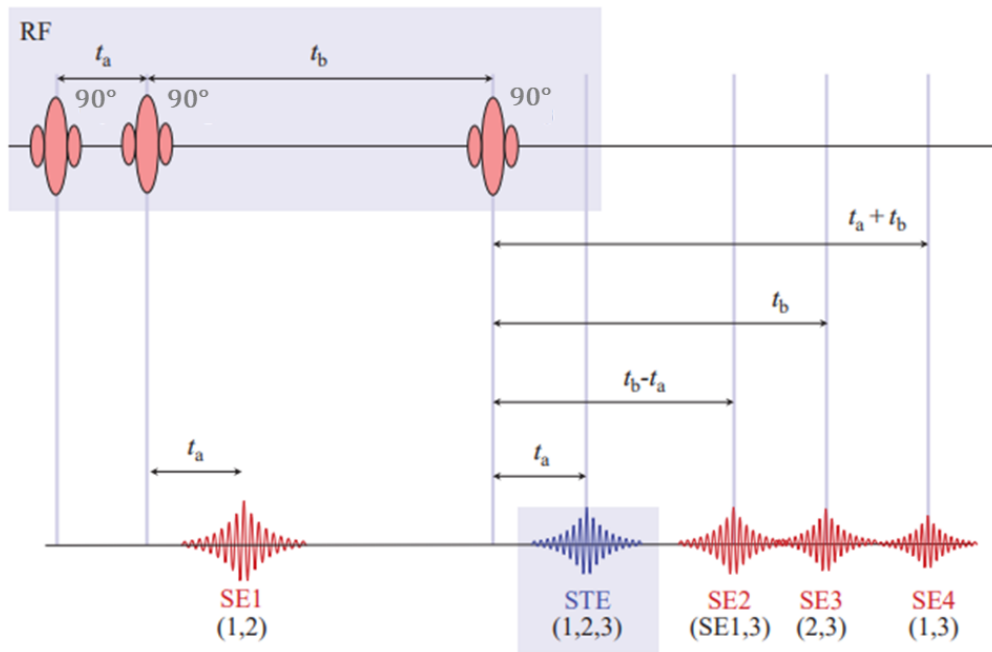
Figure 1.8: Stimulated echo formation. Three RF pulses may give rise to four Hahn echoes- SE1, SE2, SE3, and SE4 from each pair of RF pulses. SE2 is formed from the refocusing of the first echo by the third RF pulse. The stimulated echo STE is generated by all three RF pulses. The times of echo formation are given in terms of t_a and t_b, the time intervals between the RF pulses. Adapted from [27]

range of flip angle distribution across the slice. The edges of slice always receive lower flip angle than the center of the slice. RF inhomogeneity further leads to variation in flip angle. Due to imperfect refocusing of the spins, a significant z-magnetization remains at echo formation.
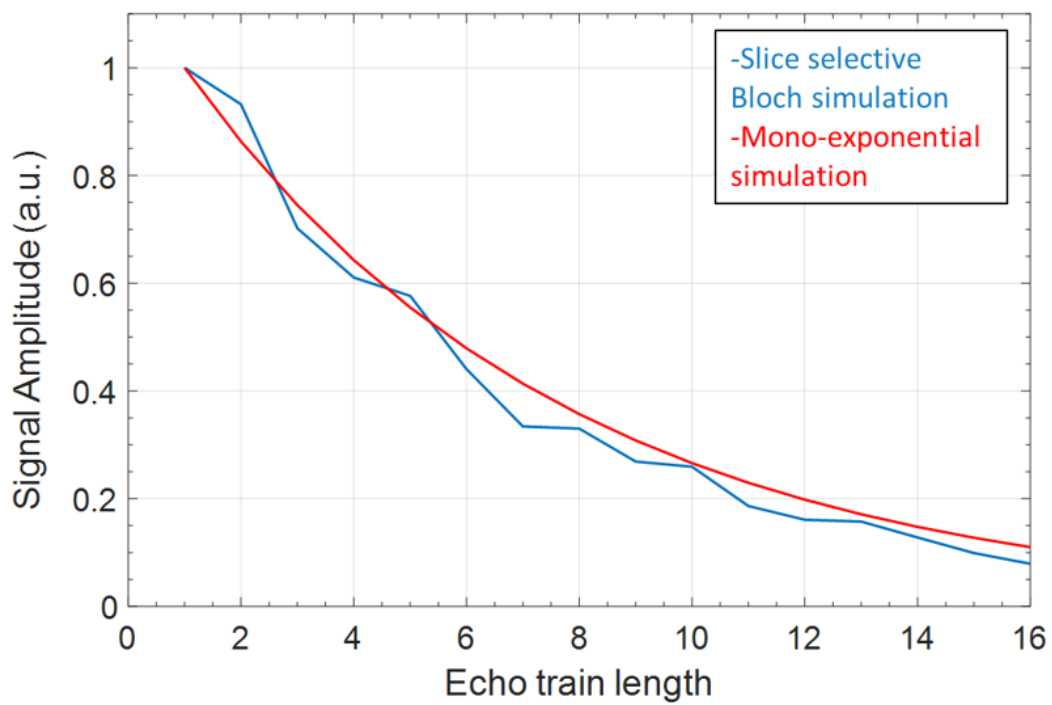
Figure 1.9: Simulated T2 decay curves with T2=72 ms. Blue curve is from from slice-selective Bloch simulation of a 2D-FSE sequence with ETL=16 and a constant flip train of 180°. Red curve is from pure exponential decay.

1.11 $B1^+$ Mapping

As described in the previous sections, at 3T and higher fields, variation in the RF transmit field, or $B1^+$ inhomogeneity results in flip angle variations across the imaging volume, leading to errors in quantitative measurements if not taken into account. $B1^+$ inhomogeneity results in differences between the nominal flip angle and the actual 'transmitted' flip angle. The transmitted flip angle can be measured by multiple methods. The Double Angle approach [28] and Bloch-Siegert Shift [29] method are most commonly used. In the double angle approach, two spin-echo images are acquired with flip angles α and 2α, respectively and a very long TR. The transmitted flip angle is then calculated as the ratio of the two signal intensities. The major shortcoming of the double angle approach is the assumption of a sinusoidal relationship between the signal and the tip angle, which is not true for non-rectangular slice profiles and non-linear magnetization response at high flip angles.

The Bloch-Siegert Shift (Figure 1.10) method encodes the $B1^+$ information into the signal phase, which removes concerns of accounting for the exact slice profile. It employs a GRE sequence with a strong off-resonance RF pulse of frequency ω_{off} applied after the excitation. ω_{off} causes a change in the precessional frequency of the spins. The off-resonance RF pulse slightly changes the effective frequency of spins that are on resonance. The slight difference in effective frequency causes the previously excited magnetization to gain phase over the duration of the RF pulse. The phase shift (ψ_{BS}) in the image is given by:

$$\psi_{BS} = \frac{(\gamma B1)^2}{2\omega_{off}} \int_0^T S(t)^2 dt \qquad (1.11)$$

$S(t)$ is the shape of the Bloch-Siegert pulse.
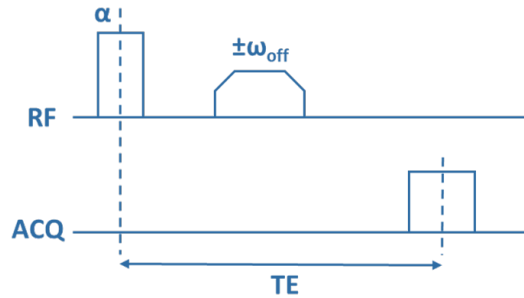
Figure 1.10: Pulse sequence diagram of a typical Bloch-Siegert sequence

Two scans are acquired at $+\omega_{off}$ and $-\omega_{off}$, enabling B1 calculation. The phase difference between both the scans gives the Bloch-Siegert phase shift, as transmit excitation and receive phases, other sequence related phases and phase shift from off-resonance $\vec{B}_0$ are same in both scans and are cancelled out.

1.12 Clinical importance of Quantitative MRI

Clinical MRI is predominantly restricted to qualitative MRI. Qualitative or weighted MRI images are preferred for their excellent contrast, high SNR and feasible scan times. Depending upon the sequence used, the same tissue can exhibit completely different signal intensities in different weighted images. The relative intensity difference between tissues lies at the core of diagnostic MRI. However, these weighted images are sensitive to many different parameters

including for example the exact flip angle used in each voxel.

Quantitative MRI is a promising tool to study tissue properties without the influence of other MR parameters. Parametric maps like T1, T2, T2* maps are expressed in absolute physical units and are ideally independent of the MR protocol as well as hardware. These maps allow a direct comparison of MR images across subjects as well as to assess specific tissue changes in longitudinal and multi-center studies. MR quantification techniques, however, often require prolonged acquisition times, show residual sensitivity to the protocol parameters, and are sometimes compromised by system imperfections. Research in quantitative MRI thus focuses on the development of fast data acquisition and post-processing techniques for accurate and precise parametric mapping of tissue properties.

1.13   T2 fitting models

1.13.1   Stimulated echo compensation with Echo Phase Graph

Accurate estimation of the underlying T2 distribution from a given signal decay curve requires the computation of realistic decay curves, one that has an apparent contribution from stimulated and indirect echoes. The extended phase graph (EPG) algorithm is one such popular approach used to approximate the longitudinal and transverse magnetization states in multi-echo sequences [26, 30–32]. EPG essentially decomposes the spin system into several dephased states: F(k) and F(-k); Z(k). k is the angular wave vector that represents a quantitative measure for dephasing. F(k) states represent the transverse magnetization, and Z(k) represents the longitudinal magnetization

component state. The minus sign indicates refocusing of F(k).These states are computed from the fourier transformation of $M(\omega)$, ω is the offset frequency.

$$F(k) = \int_{\omega} M_{xy}(\omega) \exp^{-i\omega n\tau} d\omega \qquad (1.12)$$

$$Z(k) = \int_{\omega} M_z(\omega) \exp^{-i\omega n\tau} d\omega \qquad (1.13)$$

The complete magnetization is defined by $\vec{F}$, which consists of various EPG partitions states with different k:

$$\vec{F} = F_0 \, Z_0 \, F_1 \, F_{-1} \, Z_1 \, F_2 \, F_{-2} \, Z_2 ..... F_k \, F_{-k} \, Z_k \qquad (1.14)$$

The effect of the pulses on each submatrix $[F_k \, F_{-k} \, Z_k]$ can be described by a transition matrix $T(k, \alpha_n)$ given by the following equation:

$$T(k, \alpha_n) = \begin{pmatrix} cos^2(\alpha_n/2) & sin^2(\alpha_n/2) & -sin(\alpha_n) \\ sin^2(\alpha_n/2) & cos^2(\alpha_n/2) & sin(\alpha_n) \\ -1/2sin(\alpha_n) & 1/2sin(\alpha_n) & cos(\alpha_n) \end{pmatrix} \qquad (1.15)$$

Figure 1.11 shows an example of the signal evolution with the EPG algorithm. One of this model's first assumptions is a fully dephased signal before applying the first refocusing pulse. Each successive RF pulse then splits the magnetization into different pathways. After an RF pulse, magnetization can be regarded as a composition of 3 components: a rephasing transverse component, a dephasing transverse component, and a longitudinal component. Echoes occur where phase lines cross the zero-phase line. The three echoes are: direct spin-echo (green), stimulated echo (blue), and an indirect echo (red).
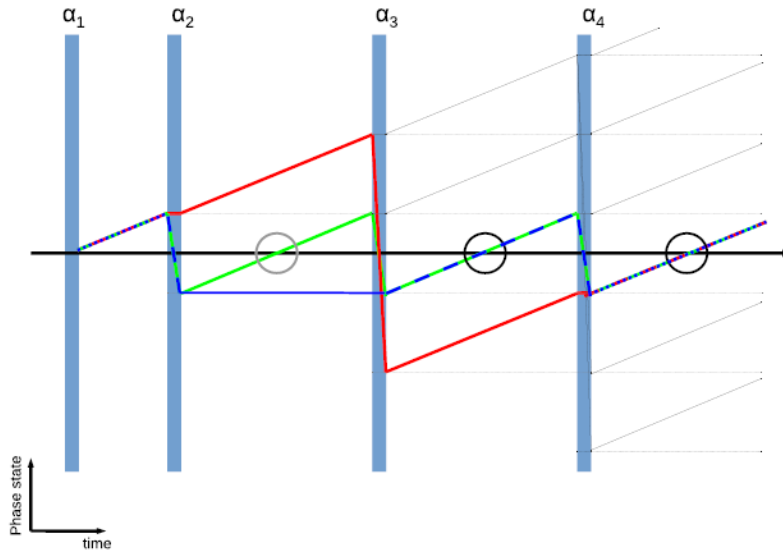
Figure 1.11: Extended Phase Graph diagram for an arbitrary four pulse spin-echo sequence. All pathways are indicated in black. Vertical lines indicate the RF pulses. Horizontal and slanted lines indicate echo pathways. Diagonal lines indicate phase evolution of transverse states, while horizontal lines indicate phase storage. Three pathways are highlighted: the green line indicates a pure spin-echo pathway, the blue line indicates a stimulated echo pathway, the red line indicates an indirect echo pathway.

1.13.2 Stimulated echo compensation with full Bloch modelling

The EPG method typically approximates the slice profile with a Fourier transform of the RF pulse shape. However, due to the non-linearity of the Bloch Equations, the Fourier transformation does not work well for large flip angles. Inaccurate slice profiles result in error in T2 quantification as the amount of stimulated echo contamination in an echo depends upon the refocusing slice profile.

We model the dual-echo FSE pulse sequence in our work by employing so-

lutions to the Bloch equations. T2 decay curves are generated using slice selective Bloch simulations with RF pulses modelled as a series of hard pulses and gradients, thus using a hard pulse approximation, as implemented in the Shinnar-Le Roux Algorithm (SLR). The SLR algorithm is based on a discrete approximation to the spin domain version of the Bloch equation. The algorithm is described in detail in [33].

In the first step of the T2 fitting routine, a dictionary of decay curves with many T2 and flip angle values was created. This dictionary of decay curves was specific to the pulse sequence parameters used to acquire the FSE data (RF pulse shapes and timings, gradient amplitudes, crusher gradients, echo spacing, and ETL). The second step involved fitting the FSE data. We provided flip angle maps to the fitting algorithm. Flip angle maps were provided as normalized $B1^+$ maps ($nB1^+$), where n is a correction factor relating the prescribed flip angle to the actual flip angle achieved at the center of the slice. Voxel-wise fitting was performed via minimization of the sum squared difference using a subset of decay curves from the dictionary with excitation and refocusing flip angles, which correspond to the voxel's measured value.

Bloch Equation Modelling

As previously described in section 1.8, Bloch equations describe the evolution of the magnetization vector $\vec{M}(t) = [M_x(t), M_y(t), M_z(t)]$ in the presence of magnetic field gradients. The Bloch Equation in the rotating frame are:

$$\frac{d}{dt}\begin{bmatrix}M_x\\M_y\\M_z\end{bmatrix}=\gamma\begin{bmatrix}0 & \vec{G}\cdot\vec{r} & -B_1 sin(\phi)\\-\vec{G}\cdot\vec{r} & 0 & B_1 cos(\phi)\\B_1 sin(\phi) & -B_1 cos(\phi) & 0\end{bmatrix}\begin{bmatrix}M_x\\M_y\\M_z\end{bmatrix}+\begin{bmatrix}(1/T2)M_x\\(1/T2)M_y\\(1/T1)(1-M_z)\end{bmatrix}$$

$$(1.16)$$

where B_1 and ϕ are the amplitude and phase of the RF pulse, $\vec{G}$ is the slice selection gradient, $\vec{r}$ is the location where G=0. Assuming T1 and T2 are long relative to the RF pulse duration, Equation 1.16 can be simplified to:

$$\frac{d}{dt}\begin{bmatrix}M_x\\M_y\\M_z\end{bmatrix}=\gamma\begin{bmatrix}0 & \vec{G}\cdot\vec{r} & -B_1 sin(\phi)\\-\vec{G}\cdot\vec{r} & 0 & B_1 cos(\phi)\\B_1 sin(\phi) & -B_1 cos(\phi) & 0\end{bmatrix}\begin{bmatrix}M_x\\M_y\\M_z\end{bmatrix}$$

$$(1.17)$$

The magnetization vectors were calculated at 1501 points equally spaced over thrice the excitation width in the slice-select direction.

RF pulse modelling

As an example of RF pulse modelling, we modelled two categories of slice-selective RF pulses, low SAR and normal SAR using the SLR algorithm. An overview of the excitation and refocusing RF pulses with their respective gradients and simulated slice profiles are shown in Figure 1.12 and Figure 1.13. While the normal SAR RF pulse is played out with a constant amplitude slice-select gradient (G_{ss}), the low SAR RF pulse is applied with a time-varying G_{ss}. The Gaussian low SAR excitation and refocusing RF pulses were 2.56 ms and 3.85 ms in duration with [0.4 1] and [0.27 0.69] as their respective

minimum and maximum slice select gradient strength in G/cm. The Gaussian normal SAR excitation and refocusing RF pulses were 3.07 ms and 2.73 ms in duration applied with a constant 0.56 G/cm and 0.44 G/cm gradient strength, respectively.

Recall from section 1.10.2 that SAR is proportional to $(B1^+)^2$. The RF pulse can be stretched in time to reduce the RF amplitude, which reduces the RF bandwidth. The reduction in RF bandwidth can be compensated by decreasing the slice-select gradient's amplitude, thus not compromising the desired slice width. RF pulses were modelled using 1024 points equally spaced over the duration of the pulse. The time-varying G_{ss} was interpolated to match the resolution of the low SAR RF pulse.
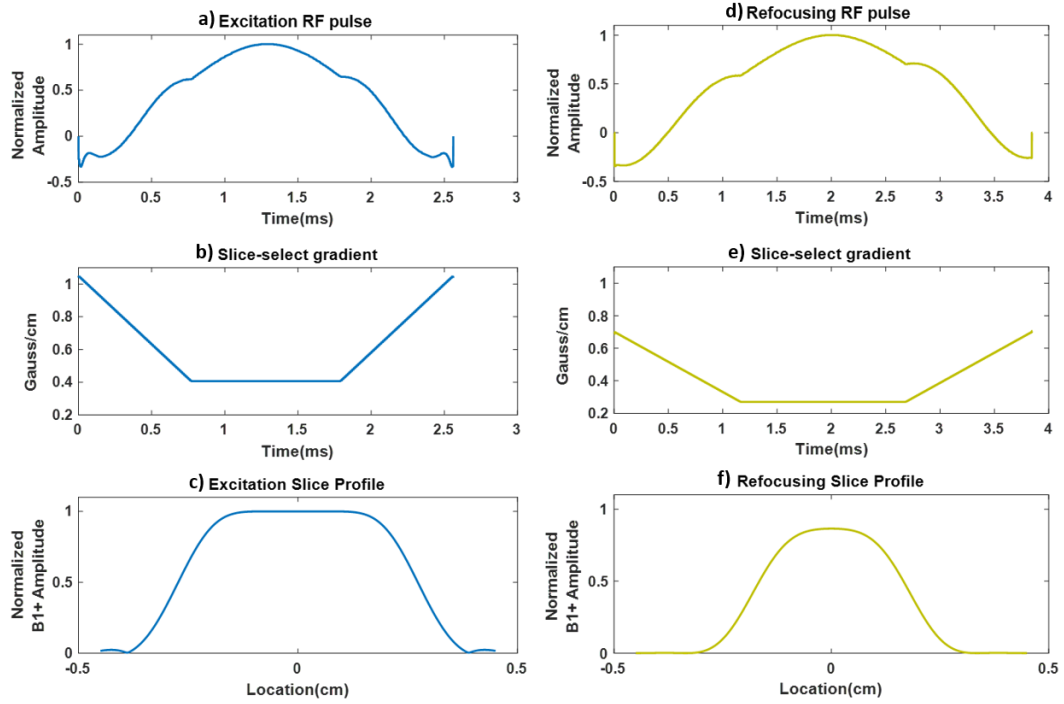
Figure 1.12: Low SAR RF pulses. (a) A 90° excitation pulse shape with its slice-select gradient (b) and (c) the resulting slice profile modelled using the SLR algorithm are shown in the first column. The second column shows (d) A 180° refocusing pulse shape with its slice-select gradient (e) and (f) the resulting slice profile modelled using the SLR algorithm. The simulation reflects parameters used for a 2D acquisition with 3 mm slice thickness.
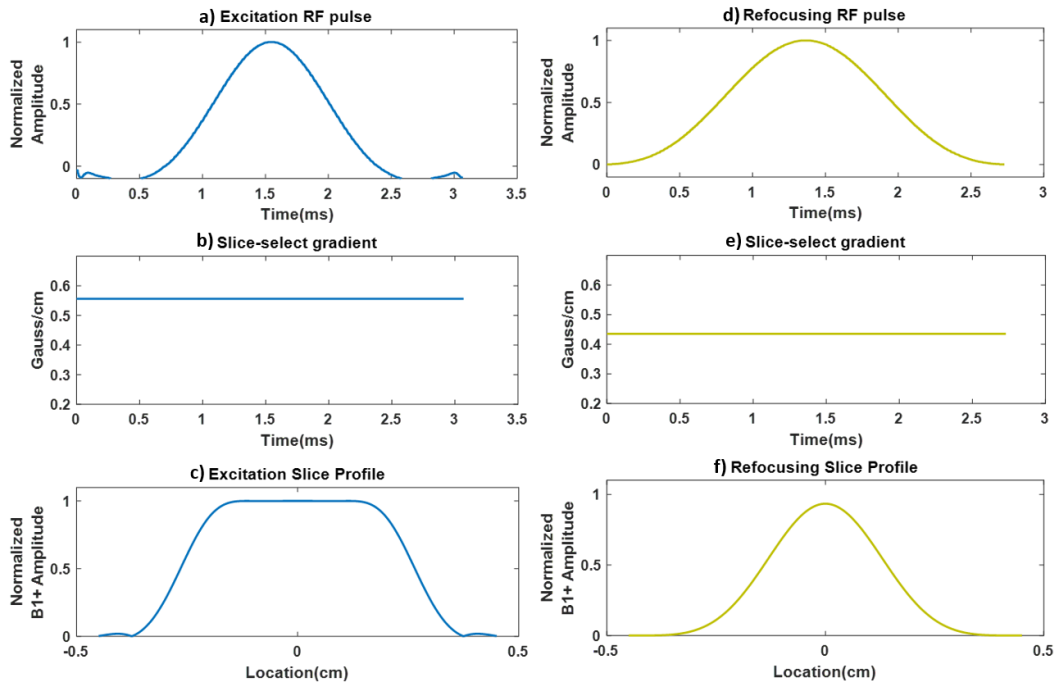
Figure 1.13: Normal SAR RF pulses. (a) A 90° excitation pulse shape with its slice-select gradient (b) and (c) the resulting slice profile modelled using the SLR algorithm are shown in the first column. The second column shows (d) A 180° refocusing pulse shape with its slice-select gradient (e) and (f) the resulting slice profile modelled using the SLR algorithm. The simulation reflects parameters used for a 2D acquisition with 3 mm slice thickness.

A comparison of the slice profiles corresponding to each type of RF pulse is illustrated in Figure 1.14. The effect of lowering G_{ss} during the peak of low SAR RF pulse resulted in a slice profile that's quite different from the one obtained with a constant G_{ss} (Fig.1.14d). As seen in Fig. 1.14, the excitation profiles are quite comparable because while the normal SAR excitation pulse was comparatively longer in duration, it was played out with a relatively higher gradient strength.
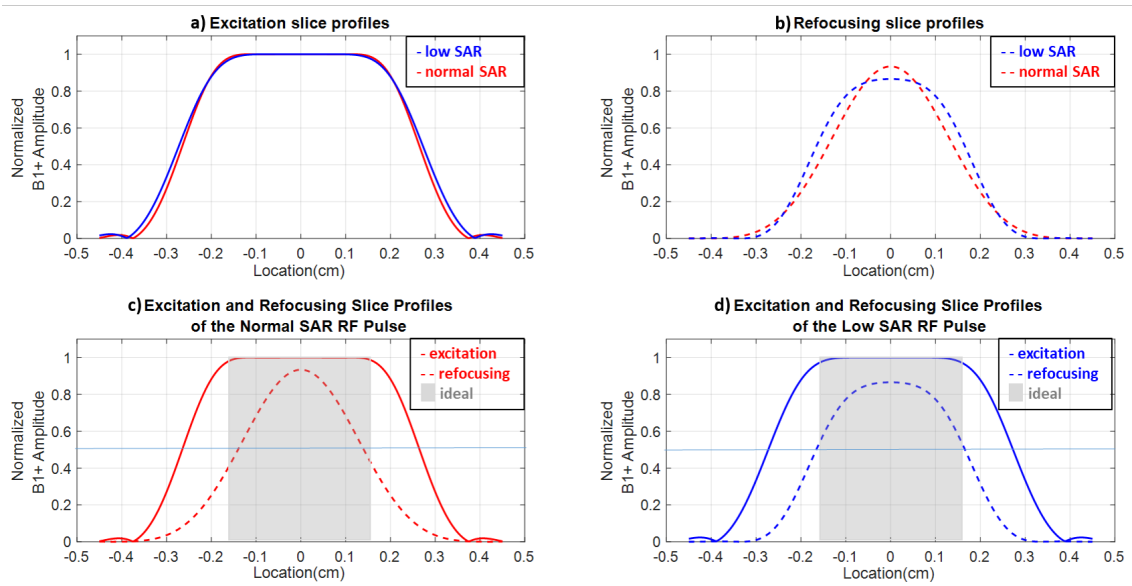
Figure 1.14: Comparing excitation and refocusing slice profiles from low SAR and normal SAR RF pulses.The excitation slice profiles in (a) are similar. The refocusing slice profile from low SAR resulted in a flatter top than the one from the normal SAR RF pulse as seen in (b). Excitation slice profiles are wider than their respective refocusing slice profiles in both c) and d)

1.14   Image processing

All brain images were skull-extracted using the Brain Extraction Tool (BET) in FMRIB Software Library (FSL v6.0). The flip angle maps were processed with a 3×3 median filter and 3-D Gaussian smoothing kernel with $\sigma = 0.6$ before T2 fitting. The flip angle maps were co-registered and resliced to the dual-echo images' native space using the within-subject rigid body registration tool in Statistical Parameter Mapping (SPM-12). Six bilateral regions of interest (Caudate, Putamen, Globus Pallidus, Thalamus, Genu, and Splenium) were chosen to compare the T2 values. An example of a T2-weighted slice overlaid with these ROIs is shown in Figure 1.15. These regions were automatically segmented using the Harvard-Oxford cortical and subcortical structural atlas for grey matter structures and Jülich histological atlas for white matter structure from FSL v6.0. High resolution T1 images were used to overlay the atlases. Careful linear and non-linear registrations were performed to transform the FSE and high resolution T1-weighted images into the MNI-152 standard space in order to define the ROIs using the atlases. All registrations and ROIs were manually inspected.
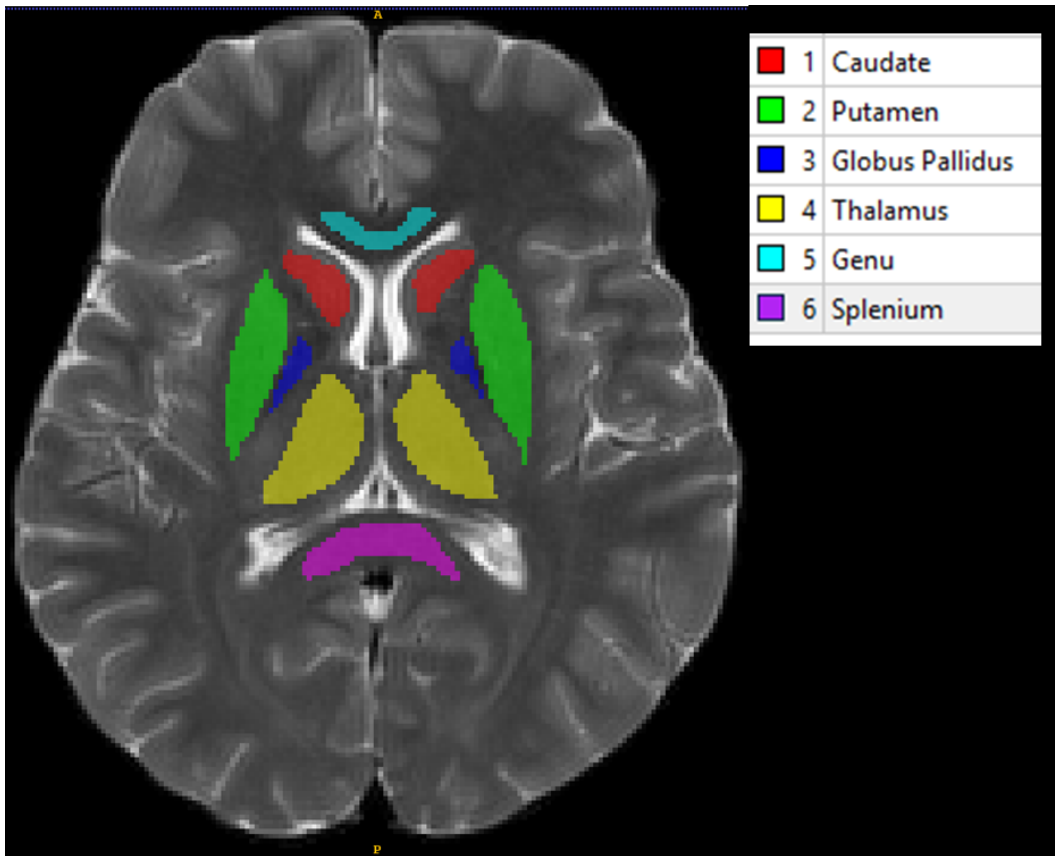
Figure 1.15: An axial slice of T2-weighted image overlaid with the ROIs

1.15 T2 relaxation in the human brain

T2 values in the literature can vary substantially depending on the methods used. Example values from the literature are shown in Table 1.1

Table 1.1: Summary of T2 relaxation studies in healthy human brain

Author Year	n mean age or age range (years)	Field Strength	T2 values (ms) mean ± std	Method
Wansapura et al. 1999 [34]	19 37.4	3T	Frontal GM: 110 ± 4 Insular GM: 102 ± 2 Parietal GM: 112 ± 4 Occipital GM: 132 ± 9 Frontal WM: 74 ± 1 Parietal WM: 80 ± 1 Occipital WM: 84 ± 1	Single slice 12 echo MESE experiment. Monoexponential fitting skipping first 2 echoes
Mädler et al. 2006 [35]	6 -	3T	Frontal WM: 69.1 ± 1.3 Parietal WM: 69.4 ± 1.1 Occipital WM: 72.3 ± 2.1 Caudate: 67.4 ± 2.7 Putamen: 65.8 ± 1.2 Thalamus: 64.3 ± 4.5 Genu: 57.3 ± 4.3 Splenium: 58.3 ± 4.2	3D 32 echo CPMG-slice selective optimized refocusing pulses.Multi-component T2 analysis with NNLS algorithm
Sedlacik et al. 2014 [36]	<40 30	3T	Frontal WM: 90.1 ± 10.8 Occiptal WM: 100 ± 9.7 Frontal Cortex: 119 ± 8.0 Occipital cortex: 125 ± 7.4 Thalamus: 94.3 ± 10.3 Putamen: 87.7 ± 9.9 Globus Pallidus: 76.3 ± 12.5 Caudate Head: 95.2 ± 9.9	3 echo mTSE sequence. Monoexponential fitting skipping first echo.
Kumar et al. 2012 [37]	60 31-66	3T	Frontal GM: 114.9 ± 17.9 Midline Occipital GM: 117.9 ± 21.9 Frontal WM: 91.7 ± 5.1 Occiptal WM: 101.6 ± 5.6 Mid-Thalamus: 85.5 ±3.5 Putamen: 77.6 ± 4.9 Globus Pallidus: 63.8 ± 6.0 Caudate Nuclei: 88.4 ± 6.8	Dual-echo TSE sequence. Two point monoexponential fitting.
Deoni 2009 [38]	4 25-34	3T	Frontal WM: 50 ± 3.75 Thalamus: 73.0 ± 9.2 Putamen: 68.8 ± 7.8 Caudate Head: 82.2 ± 9.0	DESPOT2-FM

1.16   Thesis Motivation

Raymond V. Damadian in 1971 demonstrated that cancer cells had longer T1 and T2 values than normal cells [39]. Since then, relaxation-weighted imaging has gained immense popularity in diagnostic imaging. Tissue abnormalities can also be observed in weighted images. However, in order to fully understand the mechanisms behind these abnormalities, it is crucial to study the intrinsic multi-parametric dependence of the MRI signal. Quantification of T1, T2, PD, and diffusion allows a better characterization of the tissues and pathologies. Relaxation time measurements have been shown to improve diagnosis, prognosis and monitoring of various stages of diseases, for example, in studies concerning Autism [40], Parkinson's [41], Dementia [42, 43], Multiple Sclerosis [44], Stroke [45], Tumor [46], Epilepsy [47]. It is also a promising tool to compare MR images across subjects, time-period, multi-centers, facilitating group comparisons. Due to the popularity of weighted images in clinical practice, there is a high demand for rapid quantification of relaxation maps. Authors in the past have attempted this by either directly fitting weighted images or using specialized pulse sequences [32, 48–51]. Most specialized pulse sequences are time-consuming and hence are not preferred in clinics.

In this work, we examine T2 quantification in the human brain at 3T. McPhee and Wilman [52] originally implemented retrospective quantification of T2 from PD and T2-weighted images. In Chapter 2, we extend the approach to a multi-site and multi-vendor study. We demonstrate the significance of accounting for pulse sequence differences, particularly refocusing flip train differences and $B1^+$ inhomogeneity to minimize the bias in T2 quantification from

multi-center studies. By doing so, we conclude that it is possible to enable retrospective quantitative analysis of existing weighted clinical and research data.

Chapter 2

Bloch modelling enables robust T2 mapping using retrospective Proton Density and T2-weighted images from different vendors and sites [1]

T2 quantification is commonly attempted by applying an exponential fit to proton density (PD) and transverse relaxation (T2)-weighted fast spin-echo (FSE) images. However, inter-site studies have noted systematic differences between vendors in T2 maps computed via exponential fitting due to imperfect slice refocusing, different refocusing angles and transmit field ($B1^+$) inhomogeneity. We examine T2 mapping at 3T across 13 sites and two vendors in healthy volunteers from the Alzheimer's Disease Neuroimaging Initiative (ADNI) database using both a standard exponential and a Bloch modelling approach. We show that the two-echo fitting method based on Bloch equation modelling of the pulse sequence with prior knowledge of the nominal refo-

---

cusing angles, slice profiles, and estimated $B1^+$ maps yields similar T2 values across sites and vendors by accounting for the effects of indirect and stimulated echoes. By modelling the actual refocusing angles used, T2 quantification from PD and T2-weighted images can be applied in studies across multiple sites and vendors.

2.1 Introduction

Transverse relaxation (T2) time is one of the fundamental contrast mechanisms in MRI and is highly sensitive to a wide range of tissue pathologies [53–57]. T2 mapping sequences, in general, are time-consuming and routine clinical use in the brain is rare. Furthermore, T2 mapping sequences typically have a substantial reduction in spatial resolution relative to the standard weighted images used in clinical practice [58]. Dual-echo fast spin-echo (FSE) or turbo spin-echo (TSE) sequences [11] are used in clinical MRI applications enabling high-resolution proton density (PD) and T2-weighted contrast. Many authors have attempted to estimate T2 by fitting a simple exponential decay function to the PD and T2-weighted FSE images [36, 59–61]. However, fitting with an exponential decay curve often results in inaccurate T2 values arising from three main sources of error, all of which contribute to the presence of stimulated or indirect echoes because the refocusing pulses are not ideal [26, 32, 62]. First, refocusing flip angles less than 180° are often employed in FSE sequences to mitigate specific absorption rate problems. Second, non-rectangular slice profiles lead to a variation of flip angles across the slice. Third, substantial radiofrequency (RF) interference effects occur at field strengths 3T and higher,

and to a lesser extent at lower field strengths, which causes flip angles to vary from their nominal value across the imaging volume.

In their inter-site study using the Alzheimer's Disease Neuroimaging Initiative (ADNI-1) database, Bauer et al.[59], quantified T2 from exponential fitting of the PD and T2-weighted images and compared across sites and vendors at 1.5T. They reported highly variable T2 values, concluding significant inter-site biases. However, in a two-point exponential fit using PD-weighted and T2-weighted images, the effects of stimulated echoes may go unnoticed, since the whole decay curve is not visible. Thus, the typical increased signal after the second refocusing pulse from stimulated echoes and subsequent oscillations are not seen. Different vendors or sites may use slightly different refocusing flip angle schemes leading to unaccounted biases in standard exponential fitting outputs, with large differences in resulting T2 estimates observed between sequence implementations. A more accurate two-point T2 fitting method employing Bloch simulations and RF pulse modelling in conjunction with prior knowledge of the refocusing flip angles was introduced by McPhee and Wilman [52], which builds on the general idea of stimulated echo compensation that models the actual spin response [32, 49]. The two-echo Bloch modelling approach has been applied at a single site at 1.5T to examine T2 changes in the brain over 7 years in multiple sclerosis using retrospective clinical images [63]. The goal of our current work is to examine retrospective T2 quantification in the brain across multiple sites and vendors at 3T using dual-echo FSE images from the ADNI-1 database. We show that by accounting for the differences in pulse sequences and the flip angle variation within and across slices, T2 mapping can be applied in studies across sites and vendors.

2.2 Methods

2.2.1 Data

Retrospective brain MRI exams were downloaded from the ADNI-1 database (**https://ida.loni.usc.edu/login.jsp?project=ADNI**). Inclusion criteria were healthy subjects with available 3T scans from one of two vendors: Siemens Medical Systems (vendor 1) or General Electric Healthcare (vendor 2). A total of 24 subjects were found from 13 different sites in North America from the two MRI vendors. Fourteen healthy subjects (nine female, five male, mean age 73 yrs, range 59 – 80 yrs) were scanned with MRI systems from vendor 1, and the remaining ten (six female, four male, mean age 75 yrs, range 70 – 86 years) from vendor 2. All exams used a 2D dual FSE/TSE protocol with sequence parameters as follows: TE1 10.0 – 12.8 ms, TE2 95.0 –103.0 ms, TR 3000 ms, echo train length 14 – 16, echo spacing 10.0 – 12.8 ms, 48 slices, voxel size $3.0 \times 0.94 \times 0.94 \, mm^3$, 3 concatenations, and acquisition time 5 min. Although most parameters for the 2D PD-T2 FSE were very similar, vendor 1 used a refocusing flip angle train of mainly $150°$ while vendor 2 used different refocusing flip angle trains depending on the software release that varied between sites, including a constant $125°$ refocusing angle train, and a mainly $160°$ train.

To account for receive coil effects, ADNI-1 included two rapid 3D calibration scans, one of which used the transmit body coil for both excitation and signal reception. This calibration scan enabled estimation of the normalized transmit RF field ($nB1^+$) for central brain regions, a necessary input for the Bloch simulation based T2 fitting model when given only the two PD and T2-weighted

decay data points [52]. Parameter specifications for both vendors were flip angle 2° , TE 1.1 – 1.3 ms, TR 2.9 – 3.4 ms, and 40 s acquisition time. Voxel size was $2.5 \times 2.3 \times 2.3 \, mm^3$ for vendor 1 and $2.5 \times 1.2 \times 1.2 \, mm^3$ for vendor 2.

To validate the $B1^+$ estimation method from the calibration scan, prospective acquisitions using the ADNI-1 MRI protocol were collected on a 3T Prisma (Siemens Medical Systems) for five additional healthy subjects (3 male, 2 female, mean 26 years, 21 – 31 years). These subjects received a $(B1^+)$ map acquisition using the Bloch-Siegert method [29] to serve as the gold $(B1^+)$ standard. Scan parameters for the Bloch-Siegert $(B1^+)$ mapping were as follows: TE 2.24 ms, TR 19.72 sec, voxel size $1.6 \times 1.6 \times 3.0 \, mm^3$, flip angle 5° , and acquisition time 40 sec. The estimated $B1^+$ maps from the ADNI-1 calibration scan were compared against the measured $B1^+$ maps. Prospective subjects provided written, informed consent and the local institutional ethics board approved this investigation.

2.2.2 Estimating $B1^+$ map from calibration images

We estimated $B1^+$ maps from the low flip angle calibration scan. The signal intensity, S of the calibration scan with respect to the receive RF field $(B1^-)$, transmit RF field $(B1^+)$, and scaling factor (C) for a rectangular RF pulse of duration t is given as:

$$S \propto B1^- sin(\gamma B1^+ t) \tag{2.1}$$

Noting the small flip angle of 2°

$$S \propto B1^- B1^+ \tag{2.2}$$

Further simplification can be made by making a rough assumption that for the body coil, $B1^- = B1^+$ in central brain regions at 3T [64]. Hence an approximate $B1^+$ profile can be estimated simply by $S \propto (B1^+)^2$. $B1^+$ maps were estimated for all subjects using this approach. Despite the small flip angle of $2°$ for the calibration scan, the long T1 of cerebrospinal fluid (CSF) leaves some T1 weighting, and CSF has increased proton density. However, since CSF measurements were not considered in this study, these weightings were not of concern. Nevertheless, for display purposes only, a simple CSF correction was performed to account for higher CSF PD (1.0 vs 0.8 WM/GM) and longer CSF T1 (3500 ms).

The last step in the $B1^+$ map estimation involved global scaling such that the n$B1^+$ map then corresponds to a map of scaling factors, relating flip angles achieved at each location across the volume, to the nominal flip angles used in the sequence. We assume that the mean value of this $B1^+$ across the whole brain volume is equal to 1.00 (i.e. the mean flip angle achieved across the whole brain volume is equal to the nominal flip angle used), and scale the map accordingly. The assumption that this method provides a sufficiently accurate $B1^+$ map estimate was verified from the validation subjects in comparison to the measured $B1^+$ map using difference images and profile plots.

2.2.3 T2 fitting model

T2 maps were generated from fitting of the dual-echo FSE data by modelling the actual sequence used. Bloch fitting utilized Indirect and Stimulated Echo

Compensation (ISEC), as previously described[52]. The estimated $nB1^+$ maps were provided as flip angle maps to the fitting algorithm. The method models slice-selective RF pulses using the Shinnar-Le Roux algorithm [33] and employs comprehensive Bloch simulation for pulse sequence modelling to create a dictionary of T2 decay curves. For the dictionary, simulations used a range of T2 from 10 – 1000 ms, with resolution at 0.1 ms resolution up to 150 ms, 1.0 ms from 150 – 200 ms, 2.0 ms from 200 – 300 ms, 5 ms from 300 – 500 ms, and 10 ms from 500 – 1000 ms. The longitudinal relaxation (T1) time was kept constant at 1 second, since T1 variations have very minor effects. The uniform T1 assumption for the Bloch based fitting model is evaluated in detail in McPhee and Wilman [52]. The nominal flip angles of each sequence were used along with an $nB1^+$ ranging from 0.40 – 1.40 at 0.005 resolution to account for the varying flip angle distribution across the brain due to RF interference. The dictionary of curves was specific to the pulse sequence parameters used to acquire the data. FSE data were fit for T2 and amplitude via minimization of the sum squared difference. All simulations and fitting methods were performed using in-house MATLAB (R2016b, 64 bit) code. Standard exponential fitting was also performed for comparison.

2.2.4 T2 analysis

The T2 maps were compared using whole-brain T2 histograms and manually drawn regions-of-interest (ROIs) from bilateral grey and white matter structures (Caudate, Putamen, Globus Pallidus, Thalamus, Genu, and Splenium). Mean ROI T2 values were reported, with multi-slice bilateral ROIs combined. The estimated $B1^+$ maps and measured $B1^+$ maps were co-registered and

resliced to the dual-echo images' native space using the within-subject rigid body registration tool in Statistical Parameter Mapping (SPM-12). All brain images were skull-extracted using the Brain Extraction Tool (BET) in FMRIB Software Library's (FSL v6.0).

Statistical analyses were conducted in R (version 4.0.2, 64 bit). Wilcoxon signed-rank test was used to compare the two fitting models. The validation T2 maps generated from measured and estimated $nB1^+$ maps were also compared with the same test. The Kolmogorov-Smirnov test was used to examine the whole-brain T2 histograms of the two vendors for peak T2 and T2-width (FWHM). A p-value of < 0.05 was considered statistically significant.

2.3   Results

2.3.1   Validation of T2 fitting using B1+ map estimation

An anecdotal example of $nB1^+$ maps obtained from the measured and estimated methods is shown in Fig.2.1. The two $nB1^+$ maps show reasonable agreement in central regions with larger deviations nearer the edges of the brain. Example T2 maps generated with the two $nB1^+$ maps are shown in Fig.2.2 for the same volunteer as in Fig.2.1. Similar to the $nB1^+$ maps, there is a good accordance between the T2 maps in central portions; however, differences increase towards the edges of the brain.

Whole brain T2 histograms from all five validation subjects using the two $nB1^+$ maps are shown in Fig.2.3. No significant differences were found between the average peak T2 (p=0.34) nor the FWHM (p=0.37). Mean T2 ROIs and the corresponding $nB1^+$ values from all the validation subjects are

shown in Table 2.1. For these central ROIs, no significant differences are found in T2 or $nB1^+$ values (p>0.05).
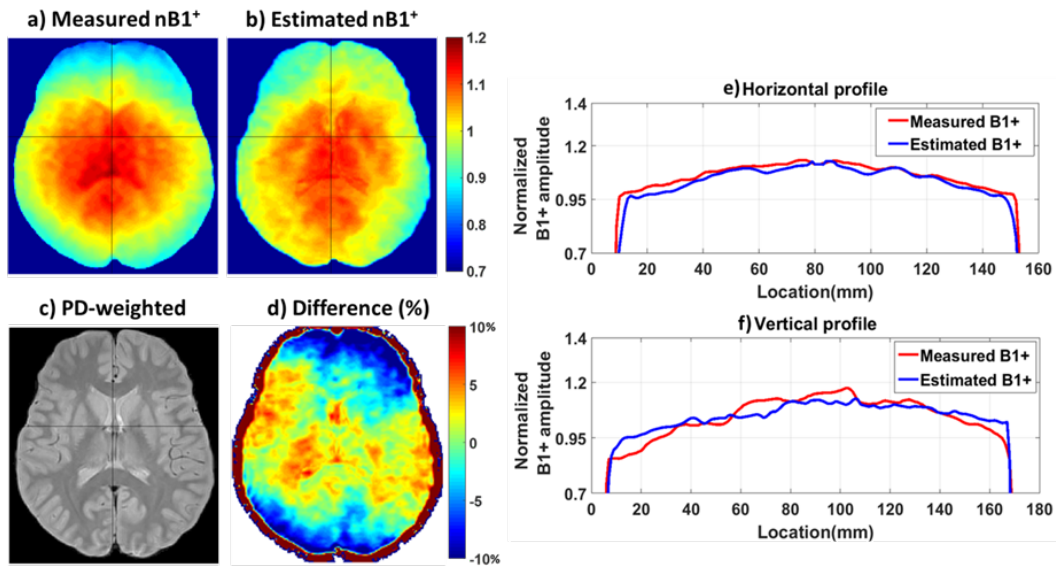
Figure 2.1: Comparison of measured $nB1^+$ map (a) and estimated $nB1^+$ map (b) of a 26 yr old healthy female volunteer. The corresponding PD-weighted axial slice (c) and percentage difference image (d), (calculated as $100\% \times (a - b)/a$) is shown. Normalized $B1^+$ map profiles obtained along the left-right and anterior-posterior directions are shown in (e) and (f) respectively.
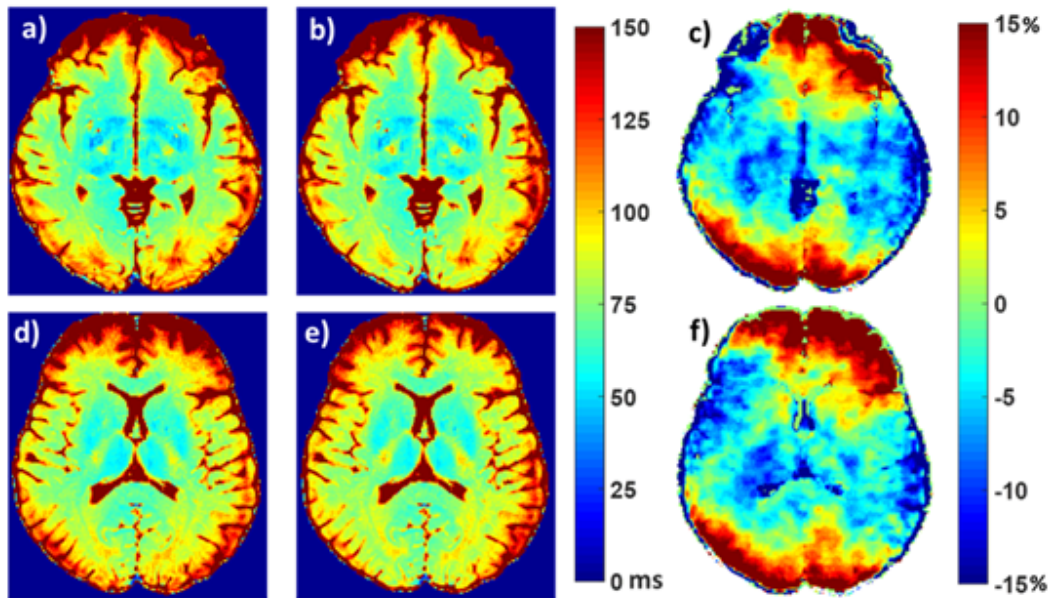
Figure 2.2: T2 maps (ms) computed with the Bloch fit method for two different slices of a healthy 26 yr old female volunteer. T2 maps created with the measured $nB1^+$ map (a,d) and the estimated $nB1^+$ map (b, e) along with the percentage difference images (c, f) are shown (calculated as $100\% \times [(measuredT2 - estimatedT2)/measuredT2)]$.
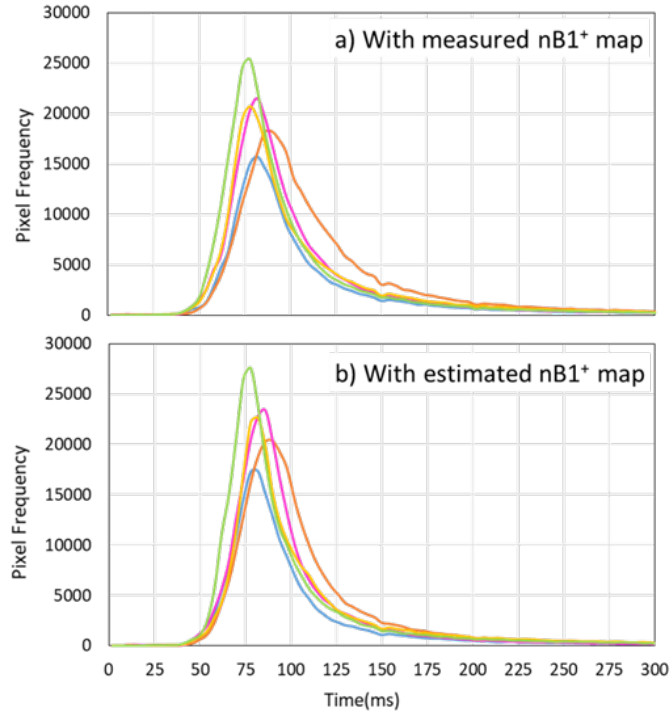
Figure 2.3: Whole-brain histograms of T2 maps from five validation subjects obtained with measured (a) and estimated (b) $nB1^+$ maps.

Table 2.1: Mean T2 (ms) and $nB1^+$ from all five volunteers

	Caudate	Putamen	Globus Pallidus	Thalamus	Genu	Splenium
measured $nB1_+$	1.06±0.02	1.09±0.02	1.12±0.02	1.14±0.03	1.00±0.02	1.11±0.02
mean T2(ms)	72.1±3.9	63.8±3.2	49.8±3.0	60.0±2.0	72.3±3.6	67.9±4.3
estimated $nB1_+$	1.08±0.01	1.09±0.02	1.11±0.02	1.12±0.02	1.01±0.02	1.08±0.01
mean T2(ms)	70.3±3.0	63.3±2.4	50.4±2.6	62.0±1.0	70.0±2.6	69.7±4.4

T2 maps were generated using the Bloch-based fit method. Data is reported as mean ± standard deviation.
n=5 volunteers, aged 26.0 ± 3.6 years.

47

2.3.2 T2 maps of ADNI-1 subjects

Example T2 maps of two different ADNI-1 subjects and their corresponding estimated $nB1^+$ maps are depicted in Fig.2.4, where the exponential fit yields very different T2 maps, while the Bloch-fit results in similar T2 maps (b,e). Vendor 1 used a refocusing flip train of 165° -150° -150° ... with an echo train length (ETL) of 14 and vendor 2 used a constant 125° flip train with ETL 16. The T2 maps displayed used PD/T2-weighted images with TE = 12, 99 ms for vendor 1, and TE = 11, 98 ms for vendor 2.

Figure 2.4: T2 maps (ms) computed using exponential method (a, d) and Bloch based fit method (b, e) for two ADNI-1 subjects, one from each vendor. Top Row: 77 yr healthy female scanned by vendor 1 using a refocusing flip train of 165° -150° -150° ... Bottom Row: 78 yr hea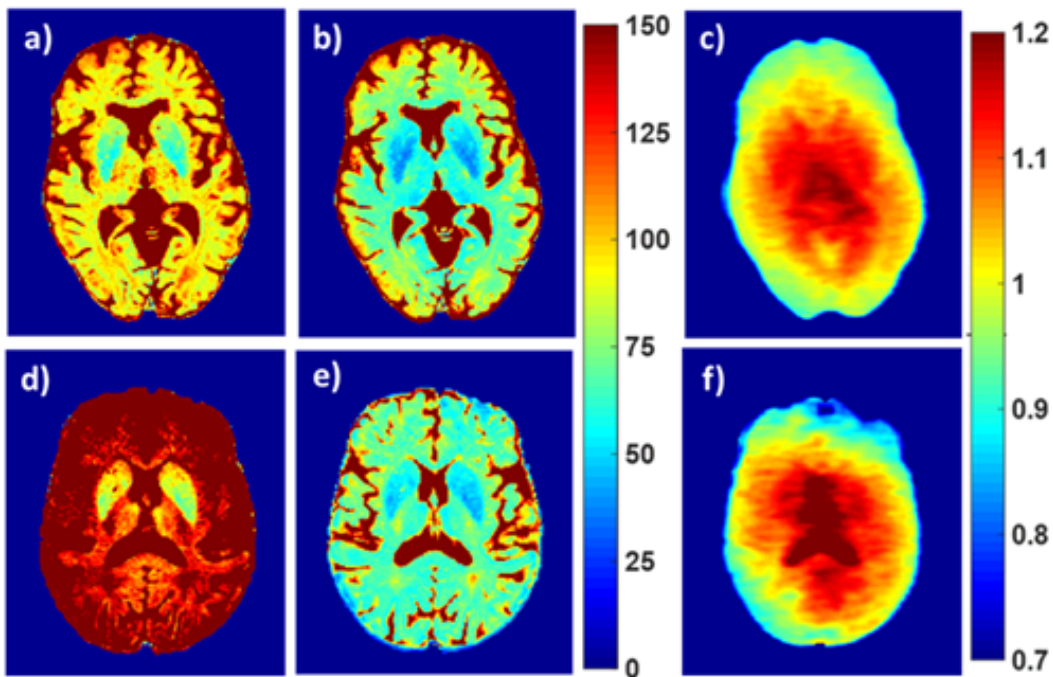lthy female scanned by vendor 2 using a refocusing flip train of 125° . Estimated $nB1^+$ maps (c, f) for each of the subjects.

Whole-brain T2 histograms from all ADNI-1 subjects from exponential and Bloch based fits are depicted in Fig.2.5 for both vendors. Histograms are clipped at 300 ms, so T2 contributions from CSF are not shown. Peak T2 from the exponential fit were higher than the corresponding peak T2 from the Bloch fit in vendor 1 (p=0.001) and vendor 2 (p=0.005). Although the subjects are different between the vendors, we still expect similar (not same) T2's between vendors as they are all healthy subjects. T2 histograms from exponential fit showed significant differences in peak T2 values between the two vendors as well (p=0.0002). On the contrary, peak T2 values between T2 histograms from Bloch fit were similar in values between the vendors (p=0.12). For each T2 histogram, the width was measured at half maximum. Exponential fit of data from vendor 2 resulted in the broadest histograms (mean histogram width of 42 ms) and highest variance between the peak T2 values (standard deviation, s = 11.5 ms). Overall analysis showed a significant width difference between the T2 fitting models for vendor 2 (p=0.006). With Bloch fit, there was no significant difference between the histogram widths of both vendors (p=0.993).

Vendor-wise mean T2 from central brain ROIs of all ADNI-1 subjects are reported in Table 2.2. The Bloch fit T2's are much shorter than the exponential fit (p=0.03) and the standard deviations are reduced. Considering all ROIs, there were no significant differences between vendors in T2 values with Bloch fit (p=0.93) nor with exponential fit (p=0.47). With the Bloch fit, the mean absolute T2 difference between vendors for all ROIs was only 3.5 ± 1.7 ms, while exponential fit was 11.1 ± 5.2 ms. Note the two groups used different subjects so exact agreement is not expected.

Table 2.2: Vendor-wise mean T2 (ms) from ADNI-1 subjects

	Vendor1		Vendor2	
Region	Exponential fit	Bloch fit	Exponential fit	Bloch fit
Caudate	84.5±5.8	54.9±2.5	100.2±9.2	60.9±4.2
Putamen	75.5±4.5	50.9±3.1	90.6±12.1	55.6±4.3
Globus Pallidus	67.0±3.0	43.7±2.3	72.7±9.1	45.6±4.6
Thalamus	92.2±5.6	56.6±2.7	96.1±8.4	59.3±3.1
Genu	88.6±5.1	64.1±3.2	103.9±10.7	61.9±3.2
Splenium	98.4±4.9	65.2±3.4	101.8±10.1	62.0±3.2

Vendor 1: n=14, aged 73.0 ± 5.5 years, and Vendor 2: n=10, aged 75.0 ± 4.2 years.

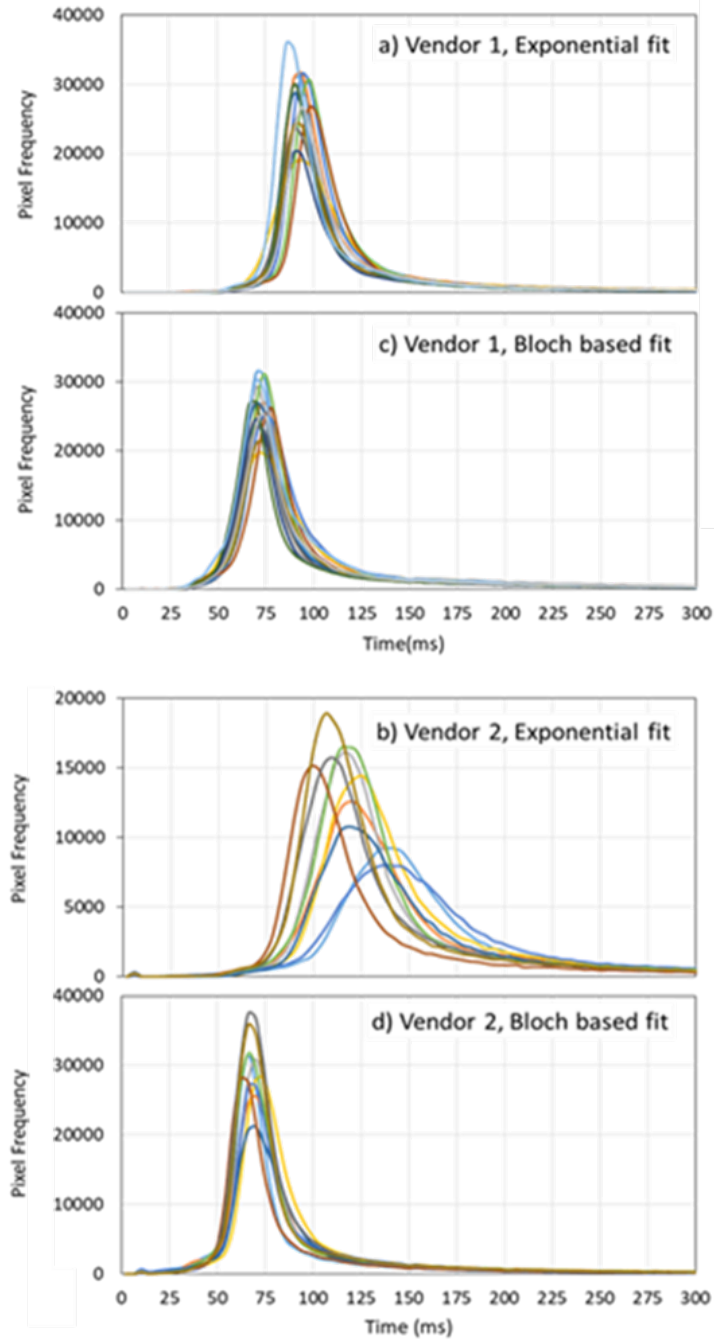Data is reported as mean ± standard deviation.

Figure 2.5: Whole-brain histograms of T2 maps from 24 ADNI-1 subjects using two vendors - 14 subjects from vendor 1 (a, c) and 10 subjects from vendor 2 (b,d). Histograms from exponential fit (a,b) and Bloch based fit (c,d). Note different scale for y-axes in (b).

2.4 Discussion

T2 maps computed with the Bloch simulation based fitting of the PD and T2-weighted images resulted in similar T2 values across vendors and sites. In contrast, T2 maps computed with an exponential fit resulted in histograms with remarkably increased peak T2 (p=0.001 for vendor 1 and p=0.005 for vendor 2) and broader FWHM for vendor 2 (p=0.006). These biases in T2 measurements were minimized by accounting for indirect and stimulated echo contamination, via modelling of the pulse sequences, using known refocusing flip angles and estimated $B1^+$ maps to account for RF field inhomogeneity. The low flip angle calibration scan of the ADNI-1 data set enabled an approximate estimation of $B1^+$ maps, which was validated in comparison to measured $B1^+$ maps in a cohort of healthy volunteers. With Bloch based fit, there were no significant differences in peak T2 (p=0.12) and FWHM (p=0.993) between the T2 maps from the two vendors.

The specific goal of our work was to demonstrate that if the differences in pulse sequences between vendors and sites are accounted for, the bias between sites/vendors can be minimized. Previous work has recognized the need for pulse sequence modelling to account for indirect and stimulated echoes, and remove T2 overestimation that is typically observed with fitting of MESE or dual-echo data with an exponential decay function [32, 49, 52]. As shown here, these T2 errors are compounded for inter-site and inter-vendor studies when RF pulse parameters vary between sites. ADNI-1 standardized most sequence timing parameters between sites and vendors with only slight variations in effective echo times, echo spacing and ETL; however, each vendor used its

own RF pulse shapes and refocusing flip angle trains. For example, vendor 1 used the same refocusing flip angle train between all of its sites, while vendor 2 used different refocusing angles that also varied between software versions. These sequence variations make standard exponential fitting unacceptable for multi-vendor T2 studies, as was found by Bauer et al.[59] with 1.5T data. More generally, to accurately simulate any 2D FSE/TSE sequence variation, the refocusing flip angle train must be known. This includes all the sequence timing parameters, the nominal refocusing angles which may vary throughout the train, the RF pulse shapes, and the relative strength of the slice select gradients for the excitation and refocusing pulses. An essential parameter is the $B1^+$ variation across the volume of interest, which must be measured, or in our case estimated. Note that for the two point fitting approach, the $B1^+$ map cannot be determined as part of the fitting process, since there are already two unknowns of initial signal and T2 value. With a supplied $B1^+$ map and the above parameters, Bloch modelling enables an accurate representation of the experimental signal decay.

T2-weighting is widely used in clinical and research studies as a marker of tissue damage, since it is sensitive (but not specific) to many biological events including water content changes, such as inflammation, tissue loss, such as neurodegeneration, and mineralization, including iron accumulation or calcification. Quantification of T2 would provide greater precision and is frequently performed in research studies, typically with MESE sequences, as well as other methods. These approaches all add additional sequences and hence additional scan time. Here we have performed T2 quantification using standard PD and T2-weighted images already available within standard studies (such as ADNI-

1). By carefully modelling the actual flip angles, it becomes possible to use this approach for T2 mapping in multi-site, multi-vendor studies.

The main limitation comes from the retrospective nature of the data. We have utilized estimated flip angle maps required for the Bloch based fitting method which only has two decay data points (PD and T2-weighted images). Although the $nB1^+$ estimation error increases towards the brain edges, the validation results showed that the estimated $nB1^+$ maps are similar in central parts of the brain and whole brain histograms were not impacted. Nevertheless we focused our ROI measures on central brain regions where the calibration assumption of body coil transmit $B1^+$ and body coil receive $B1^-$ equivalency is more accurate. While the ADNI-1 calibration scan was sufficient to estimate $B1^+$, prospective studies could use a rapid $B1^+$ mapping technique for greater precision. The slow variation of $B1^+$ in the head allows for low resolution $B1^+$ maps, which can now be acquired rapidly [65].

2.5   Conclusion

We examined retrospective T2 mapping across multiple sites and two vendors using standard PD and T2-weighted images of brain. With standard exponential fitting, large T2 biases were observed between vendors. By using Bloch-based modelling of the pulse sequence and estimating the B1+ field, biases in T2 values between sites and vendors were minimized. The use of standard PD and T2-weighted images enables quantitative T2 measurement at the same spatial resolution as standard weighted images with no additional imaging time. Bloch modelling of the actual refocusing angles enables T2

quantification from PD and T2-weighted images across multiple sites and vendors.

2.6 Acknowledgement

ern California. ADNI data are disseminated by the Laboratory for Neuro Imaging at the University of Southern California.

Chapter 3

Conclusions

3.1 Summary of main findings

Multi-echo spin-echo MRI sequences are the standard choice for measuring T2 relaxation time. These sequences typically generate multiple echoes in order to estimate T2. Due to its ease of implementation, most people still rely on a simple exponential least-squares fit through the echoes to quantify T2 from the MESE data. However, the standard exponential fitting does not account for the sources of stimulated echo contamination in a typical MESE signal. Imperfect refocusing caused by non-180° refocusing pulses, non-ideal slice profiles and $B1^+$ inhomogeneities give rise to multiple echo pathways that contaminate the MESE signal. Over the years, multiple sophisticated T2 fitting routines have been developed [31, 32, 49]; these routines aim to model all possible echo pathways in a multi-echo spin-echo sequence to compensate for the stimulated and indirect echo contamination. The EPG based methods are the most popular ones. However, the EPG approach has significant drawbacks in regards to utilizing an inaccurate slice profile model.

We show that the errors in T2 estimation from multi-site data compounded

upon using the exponential fit model. The two-point fitting method utilized in this work comprehensively models the signal decay curves by total pulse sequence modelling using Bloch equations, and accounting for the slice profiles by modelling RF pulses using the SLR-algorithm, using nominal RF flip angles and flip angle maps . Human brain T2 values obtained from the two echo FSE method with the bloch based fitting method has been shown to be in good agreement with the T2 results from the bloch based fitting of the 32 echo MESE dataset at 4.7T [52]. Our work focused on retrospective T2 mapping from dual-echo FSE clinical images at 3T. We observed significantly large differences in T2 values between vendors using the exponential fitting method. We showed that these differences could be minimized with our fitting approach. Thus any multi-site or multi-vendor studies must take into account any pulse sequence variations and use proper modelling for fitting the signal decay.

3.2   Limitations

The main limitation of this work is the unavailability of accurate $B1^+$ maps. We estimated the $B1^+$ maps in our work. These estimated $B1^+$ maps showed higher deviations towards the brain's edges, which resulted in small errors in T2 estimation. Being a two-point fitting approach, it is not possible to esti-mate T2 and $B1^+$ simultaneously, which can be done when multiple echoes are available. $B1^+$ maps can be acquired very quickly nowadays and could be included in prospective studies.

A second limitation is the two-point fitting model which is theoretically more sensitive to noise and artifacts in the data. While a many echo MESE approach

is preferred for accurate T2 mapping, it is unrealistic in a clinical setting. Hence our work takes advantage of already-in-use clinical sequences. While not as precise as MESE sequences, the two point fit provides a substantial improvement over just weighted images, enabling quantitative MRI.Furthermore, measurements within ROIs often average many pixels and signal-to-noise limitations are thus reduced.

A third limitation is the model assumes single component relaxation, which is not valid for the majority of brain tissues, which may also contain small amounts of myelin water [23]. In brain white matter, especially, the accuracy of T2 characterization using a mono-exponential model has been shown to be insufficient to account for myelin water and quite sensitive to echo timings. However, multiple component T2 fitting demands many echoes (typically 32) and low resolution to cope with fitting a large number of unknowns for each voxel. Unfortunately, the resulting myelin water T2 spectrum is unstable and researchers now only report the myelin water fraction, to avoid this deficit. Thus while the multiple component nature of the tissue is ignored, single component fitting still provides useful measures of tissue change, and most importantly single component fits can be achieved from clinical MRI methods like the dual echo with Proton density and T2-weighting.

A fourth limitation is the model assumed a constant T1 of 1 second. However, it has been shown in the past that for a large (T1/T2) values > 10 [32], the assumption will lead to only small errors. Nevertheless, we haven't validated the T1 assumption in the full range of FSE sequences that include use of lower refocusing angles and hence with varying contribution from the stimulated echoes. Future work could include T1 measurement, or at least seg-

menting white, grey matter and CSF and applying unique literature T1's to each. Lastly, note that CSF was not considered in this work, as its extremely long T2 (and T1) is not conducive to two point fitting with longest echo time being only ~ 100 ms.

3.3 Future Work

Weighted images are frequently acquired in the clinic and research. Since most of the T2 quantifying pulse sequences are time-consuming and compromising in terms of the spatial resolution, there is a rising demand for rapid and accurate quantification of MR parameters from weighted images. PD-w and T2-w data are often acquired in brain studies. By incorporating a rapid $B1^+$ map acquisition (10-12s) [65], such studies can benefit from retrospective T2 analysis with a minimal time penalty. Additionally, if $B1^+$ variation across the head can be predicted, then the fitting routine can be used to quantify T2 from existing PD/T2-w studies without a $B1^+$ map. The fitting routine can also be optimized to improve accuracies with different multi-slice acquisition schemes and possibly extended to fit for 3D data.Thus the future directions could be applying T2 mapping to any study that uses PD-w and T2-w images. Overall, the thesis aimed to demonstrate that in order to compare quantitative relaxation times across multi-center studies including different vendors, the differences in pulse sequences and imperfect refocusing should be appropriately accounted. T2 maps obtained from this model can enable valuable comparisons between multi-centric groups or changes over time in individuals or groups.

Bibliography

[1] M. A. Bernstein, K. F. King, and X. J. Zhou, *Handbook of MRI pulse sequences*. Elsevier, 2004.

[2] R. W. Brown, Y.-C. N. Cheng, E. M. Haacke, M. R. Thompson, and R. Venkatesan, *Magnetic resonance imaging: physical principles and sequence design*. John Wiley & Sons, 2014.

[3] P. Tofts, *Quantitative MRI of the brain: measuring changes caused by disease*. John Wiley & Sons, 2005.

[4] A. Abragam, *The principles of nuclear magnetism*, 32. Oxford university press, 1961.

[5] F. Bloch, "Nuclear induction," *Physical review*, vol. 70, no. 7-8, p. 460, 1946.

[6] K. Murase and N. Tanki, "Numerical solutions to the time-dependent bloch equations revisited," *Magnetic resonance imaging*, vol. 29, no. 1, pp. 126–131, 2011.

[7] S. C. Deoni, "Magnetic resonance relaxation and quantitative measurement in the brain," in *Magnetic Resonance Neuroimaging*, Springer, 2011, pp. 65–108.

[8] E. L. Hahn, "Spin echoes," *Physical review*, vol. 80, no. 4, p. 580, 1950.

[9] H. Y. Carr and E. M. Purcell, "Effects of diffusion on free precession in nuclear magnetic resonance experiments," *Physical review*, vol. 94, no. 3, p. 630, 1954.

[10] S. Meiboom and D. Gill, "Modified spin-echo method for measuring nuclear relaxation times," *Review of scientific instruments*, vol. 29, no. 8, pp. 688–691, 1958.

[11] J. Hennig, A Nauerth, and H. Friedburg, "Rare imaging: A fast imaging method for clinical mr," *Magnetic resonance in medicine*, vol. 3, no. 6, pp. 823–833, 1986.

[12] S. Duchesne, I. Chouinard, O. Potvin, V. S. Fonov, A. Khademi, R. Bartha, P. Bellec, D. L. Collins, M. Descoteaux, R. Hoge, *et al.*, "The canadian dementia imaging protocol: Harmonizing national cohorts," *Journal of Magnetic Resonance Imaging*, vol. 49, no. 2, pp. 456–465, 2019.

[13] "Consortium of ms centers, mri protocol and clinical guidelines for the diagnosis and follow-up of ms," 2018, https://cdn.ymaws.com/mscare.site-ym.com/resource/collection/9C5F19B9-3489-48B0-A54B-623A1ECEE07B/2018MRIGuidelines_booklet_with_final_changes_0522.pdf.

[14] A. Chong, R. V. Chandra, K. Chuah, E. Roberts, and S. Stuckey, "Proton density mri increases detection of cervical spinal cord multiple sclerosis lesions compared with t2-weighted fast spin-echo," *American Journal of Neuroradiology*, vol. 37, no. 1, pp. 180–184, 2016.

[15] S. Trip and D. Miller, "Imaging in multiple sclerosis," *Journal of Neurology, Neurosurgery & Psychiatry*, vol. 76, no. suppl 3, pp. iii11–iii18, 2005.

[16] F. Roemer, M. K. Javaid, A Guermazi, M Thomas, A Kiran, R Keen, L King, and N. Arden, "Anatomical distribution of synovitis in knee osteoarthritis and its association with joint effusion assessed on non-enhanced and contrast-enhanced mri," *Osteoarthritis and cartilage*, vol. 18, no. 10, pp. 1269–1274, 2010.

[17] P. S. Tofts, "Standing waves in uniform water phantoms," *Journal of Magnetic Resonance, Series B*, vol. 104, no. 2, pp. 143–147, 1994.

[18] C. M. Collins, W. Liu, W. Schreiber, Q. X. Yang, and M. B. Smith, "Central brightening due to constructive interference with, without, and despite dielectric resonance," *Journal of Magnetic Resonance Imaging: An Official Journal of the International Society for Magnetic Resonance in Medicine*, vol. 21, no. 2, pp. 192–196, 2005.

[19] B. L. Schmitz, A. J. Aschoff, M. H. Hoffmann, and G. Grön, "Advantages and pitfalls in 3t mr brain imaging: A pictorial review," *American journal of neuroradiology*, vol. 26, no. 9, pp. 2229–2237, 2005.

[20] R. J. Stafford, "High field mri: Technology, applications, safety, and limitations," in *46th AAPM Annual Meeting, American Association of Physicists in Medicine*, 2004.

[21] "Mhra mri safety guidance: Review of key changes and emerging issues," 2015, https://assets.publishing.service.gov.uk/government/uploads/system/uploads/attachment_data/file/476931/MRI_guidance_2015_-_4-02d1.pdf.

[22] R. Henkelman, G. Stanisz, and S. Graham, "Magnetization transfer in mri: A review," *NMR in Biomedicine: An International Journal Devoted*

to the Development and Application of Magnetic Resonance In Vivo, vol. 14, no. 2, pp. 57–64, 2001.

[23]   I. M. Vavasour, K. P. Whittall, D. K. Li, and A. L. MacKay, "Different magnetization transfer effects exhibited by the short and long t2 components in human brain," *Magnetic Resonance in Medicine: An Official Journal of the International Society for Magnetic Resonance in Medicine*, vol. 44, no. 6, pp. 860–866, 2000.

[24]   M. Weigel, G. Helms, and J. Hennig, "Investigation and modeling of magnetization transfer effects in two-dimensional multislice turbo spin echo sequences with low constant or variable flip angles at 3 t," *Magnetic Resonance in Medicine: An Official Journal of the International Society for Magnetic Resonance in Medicine*, vol. 63, no. 1, pp. 230–234, 2010.

[25]   K. P. Whittall, A. L. Mackay, D. A. Graeb, R. A. Nugent, D. K. Li, and D. W. Paty, "In vivo measurement of t2 distributions and water contents in normal human brain," *Magnetic resonance in medicine*, vol. 37, no. 1, pp. 34–43, 1997.

[26]   J. Hennig, "Echoes—how to generate, recognize, use or avoid them in mr-imaging sequences. part ii: Echoes in imaging sequences," *Concepts in Magnetic Resonance*, vol. 3, no. 4, pp. 179–192, 1991.

[27]   D. W. McRobbie, E. A. Moore, M. J. Graves, and M. R. Prince, "Acronyms anonymous ii: Gradient echo," in *MRI from Picture to Proton*, 3rd ed. Cambridge University Press, 2017, 207–224. DOI: 10.1017/9781107706958.014.

[28]   R. Stollberger and P. Wach, "Imaging of the active b1 field in vivo," *Magnetic resonance in medicine*, vol. 35, no. 2, pp. 246–251, 1996.

[29] L. I. Sacolick, F. Wiesinger, I. Hancu, and M. W. Vogel, "B1 mapping by bloch-siegert shift," *Magnetic resonance in medicine*, vol. 63, no. 5, pp. 1315–1322, 2010.

[30] J. Hennig, "Multiecho imaging sequences with low refocusing flip angles," *Journal of Magnetic Resonance (1969)*, vol. 78, no. 3, pp. 397–407, 1988.

[31] M. Weigel, "Extended phase graphs: Dephasing, rf pulses, and echoes-pure and simple," *Journal of Magnetic Resonance Imaging*, vol. 41, no. 2, pp. 266–295, 2015.

[32] R. M. Lebel and A. H. Wilman, "Transverse relaxometry with stimulated echo compensation," *Magnetic resonance in medicine*, vol. 64, no. 4, pp. 1005–1014, 2010.

[33] J. Pauly, P. Le Roux, D. Nishimura, and A. Macovski, "Parameter relations for the shinnar-le roux selective excitation pulse design algorithm (nmr imaging)," *IEEE transactions on medical imaging*, vol. 10, no. 1, pp. 53–65, 1991.

[34] J. P. Wansapura, S. K. Holland, R. S. Dunn, and W. S. Ball Jr, "Nmr relaxation times in the human brain at 3.0 tesla," *Journal of Magnetic Resonance Imaging: An Official Journal of the International Society for Magnetic Resonance in Medicine*, vol. 9, no. 4, pp. 531–538, 1999.

[35] B Mädler, T Harris, and A. MacKay, "3d-relaxometry—quantitative t1 and t2 brain mapping at 3t," in *Proceedings of the 14th scientific meeting, International Society for Magnetic Resonance in Medicine, Seattle, USA*, vol. 14, 2006, p. 958.

[36] J. Sedlacik, K. Boelmans, U Löbel, B. Holst, S. Siemonsen, and J. Fiehler, "Reversible, irreversible and effective transverse relaxation rates in normal aging brain at 3 t," *Neuroimage*, vol. 84, pp. 1032–1041, 2014.

[37] R. Kumar, S. Delshad, M. A. Woo, P. M. Macey, and R. M. Harper, "Age-related regional brain t2-relaxation changes in healthy adults," *Journal of Magnetic Resonance Imaging*, vol. 35, no. 2, pp. 300–308, 2012.

[38] S. C. Deoni, "Transverse relaxation time (t2) mapping in the brain with off-resonance correction using phase-cycled steady-state free precession imaging," *Journal of Magnetic Resonance Imaging: An Official Journal of the International Society for Magnetic Resonance in Medicine*, vol. 30, no. 2, pp. 411–417, 2009.

[39] R. Damadian, "Tumor detection by nuclear magnetic resonance," *Science*, vol. 171, no. 3976, pp. 1151–1153, 1971.

[40] N. Boddaert, M. Zilbovicius, A. Philipe, L. Robel, M. Bourgeois, C. Barthélemy, D. Seidenwurm, I. Meresse, L. Laurier, I. Desguerre, *et al.*, "Mri findings in 77 children with non-syndromic autistic disorder," *PloS one*, vol. 4, no. 2, e4415, 2009.

[41] D. Dexter, A Carayon, F Javoy-Agid, Y Agid, F. Wells, S. Daniel, A. Lees, P Jenner, and C. Marsden, "Alterations in the levels of iron, ferritin and other trace metals in parkinson's disease and other neurodegenerative diseases affecting the basal ganglia," *Brain*, vol. 114, no. 4, pp. 1953–1975, 1991.

[42] X. Tang, F. Cai, D.-X. Ding, L.-L. Zhang, X.-Y. Cai, and Q. Fang, "Magnetic resonance imaging relaxation time in alzheimer's disease," *Brain research bulletin*, vol. 140, pp. 176–189, 2018.

[43] G. Bartzokis, D. Sultzer, J. Cummings, L. E. Holt, D. B. Hance, V. W. Henderson, and J. Mintz, "In vivo evaluation of brain iron in alzheimer disease using magnetic resonance imaging," *Archives of general psychiatry*, vol. 57, no. 1, pp. 47–53, 2000.

[44] H. Larsson, J Frederiksen, J Petersen, A Nordenbo, I Zeeberg, O Henriksen, and J Olesen, "Assessment of demyelination, edema, and gliosis by in vivo determination of t1 and t2 in the brain of patients with acute attack of multiple sclerosis," *Magnetic resonance in medicine*, vol. 11, no. 3, pp. 337–348, 1989.

[45] Y. Wang, G. Liu, D. Hong, F. Chen, X. Ji, and G. Cao, "White matter injury in ischemic stroke," *Progress in neurobiology*, vol. 141, pp. 45–60, 2016.

[46] S. Lescher, A. Jurcoane, A. Veit, O. Bähr, R. Deichmann, and E. Hattingen, "Quantitative t1 and t2 mapping in recurrent glioblastomas under bevacizumab: Earlier detection of tumor progression compared to conventional mri," *Neuroradiology*, vol. 57, no. 1, pp. 11–20, 2015.

[47] D. Wagnerová, V Herynek, M Dezortová, P Marusič, P Kršek, J Zamecnik, F Jiru, A Škoch, and M Hájek, "The relationships between quantitative mr parameters in hippocampus in healthy subjects and patients with temporal lobe epilepsy.," *Physiological Research*, vol. 64, no. 3, 2015.

[48] M. N. Uddin, R Marc Lebel, and A. H. Wilman, "Transverse relaxometry with reduced echo train lengths via stimulated echo compensation," *Magnetic resonance in medicine*, vol. 70, no. 5, pp. 1340–1346, 2013.

[49] N. Ben-Eliezer, D. K. Sodickson, and K. T. Block, "Rapid and accurate t2 mapping from multi–spin-echo data using bloch-simulation-based reconstruction," *Magnetic resonance in medicine*, vol. 73, no. 2, pp. 809–817, 2015.

[50] C. Huang, A. Bilgin, T. Barr, and M. I. Altbach, "T2 relaxometry with indirect echo compensation from highly undersampled data," *Magnetic Resonance in Medicine*, vol. 70, no. 4, pp. 1026–1037, 2013.

[51] W. Rooney, J Pollaro, S. Forbes, D. Wang, K Vandenborne, and G. Walter, "Application of the extended phase graph technique to improve t2 quantitation across sites," in *Proc Intl Soc Mag Reson Med*, vol. 19, 2011, p. 138.

[52] K. C. McPhee and A. H. Wilman, "T2 quantification from only proton density and t2-weighted mri by modelling actual refocusing angles," *NeuroImage*, vol. 118, pp. 642–650, 2015.

[53] G. Bartzokis, D. Sultzer, P. H. Lu, K. H. Nuechterlein, J. Mintz, and J. L. Cummings, "Heterogeneous age-related breakdown of white matter structural integrity: Implications for cortical "disconnection" in aging and alzheimer's disease," *Neurobiology of aging*, vol. 25, no. 7, pp. 843–851, 2004.

[54] A. MacKay, C. Laule, I. Vavasour, T. Bjarnason, S. Kolind, and B. Mädler, "Insights into brain microstructure from the t2 distribution," *Magnetic resonance imaging*, vol. 24, no. 4, pp. 515–525, 2006.

[55] J. F. Schenck and E. A. Zimmerman, "High-field magnetic resonance imaging of brain iron: Birth of a biomarker?" *NMR in Biomedicine: An International Journal Devoted to the Development and Application of Magnetic Resonance In Vivo*, vol. 17, no. 7, pp. 433–445, 2004.

[56] E. Stephenson, N. Nathoo, Y. Mahjoub, J. F. Dunn, and V. W. Yong, "Iron in multiple sclerosis: Roles in neurodegeneration and repair," *Nature Reviews Neurology*, vol. 10, no. 8, p. 459, 2014.

[57] J. Vymazal, A. Righini, R. A. Brooks, M. Canesi, C. Mariani, M. Leonardi, and G. Pezzoli, "T1 and t2 in the brain of healthy subjects, patients with parkinson disease, and patients with multiple system atrophy: Relation to iron content," *Radiology*, vol. 211, no. 2, pp. 489–495, 1999.

[58] J. I. Hamilton, Y. Jiang, Y. Chen, D. Ma, W.-C. Lo, M. Griswold, and N. Seiberlich, "Mr fingerprinting for rapid quantification of myocardial t1, t2, and proton spin density," *Magnetic resonance in medicine*, vol. 77, no. 4, pp. 1446–1458, 2017.

[59] C. M. Bauer, H. Jara, R. Killiany, A. D. N. Initiative, *et al.*, "Whole brain quantitative t2 mri across multiple scanners with dual echo fse: Applications to ad, mci, and normal aging," *Neuroimage*, vol. 52, no. 2, pp. 508–514, 2010.

[60] D. Kim, J. H. Jensen, E. X. Wu, S. S. Sheth, and G. M. Brittenham, "Breathhold multiecho fast spin-echo pulse sequence for accurate r2 measurement in the heart and liver," *Magnetic Resonance in Medicine: An Official Journal of the International Society for Magnetic Resonance in Medicine*, vol. 62, no. 2, pp. 300–306, 2009.

[61] M. J. Knight, B. McCann, D. Tsivos, E. Couthard, and R. A. Kauppinen, "Quantitative t 1 and t 2 mri signal characteristics in the human brain: Different patterns of mr contrasts in normal ageing," *Magnetic Resonance Materials in Physics, Biology and Medicine*, vol. 29, no. 6, pp. 833–842, 2016.

[62] S Majumdar, S. Orphanoudakis, A Gmitro, M O'donnell, and J. Gore, "Errors in the measurements of t2 using multiple-echo mri techniques. i. effects of radiofrequency pulse imperfections," *Magnetic resonance in medicine*, vol. 3, no. 3, pp. 397–417, 1986.

[63] M. N. Uddin, K. C. McPhee, G. Blevins, and A. H. Wilman, "Recovery of accurate t2 from historical 1.5 tesla proton density and t2-weighted images: Application to 7-year t2 changes in multiple sclerosis brain," *Magnetic resonance imaging*, vol. 37, pp. 21–26, 2017.

[64] M. V. Vaidya, C. M. Collins, D. K. Sodickson, R. Brown, G. C. Wiggins, and R. Lattanzi, "Dependence of b1- and b1+ and field patterns of surface coils on the electrical properties of the sample and the mr operating frequency," *Concepts in Magnetic Resonance Part B: Magnetic Resonance Engineering*, vol. 46, no. 1, pp. 25–40, 2016.

[65] A. Lesch, M. Schlöegl, M. Holler, K. Bredies, and R. Stollberger, "Ultrafast 3d bloch–siegert b-mapping using variational modeling," *Magnetic resonance in medicine*, vol. 81, no. 2, pp. 881–892, 2019.